1
2
3 # Numerical Case Study of the Aerosol-Cloud-Interactions in Warm Boundary Layer Clouds over the Eastern North Atlantic with an Interactive Chemistry Module
6
7
8
9

10 Hsiang-He Lee[1], Xue Zheng[1], Shaoyue Qiu[1], and Yuan Wang[2]
11
12
13 [1]Atmospheric, Earth, and Energy Division, Lawrence Livermore National Laboratory, Livermore, CA, U.S.A.
15 [2]Department of Earth System Science, Stanford University, Stanford, CA, U.S.A.
16
17
18
19
20
21
22
23
24
25
26
27
28
29
30
31
32

37

38 *Corresponding author address: Dr. Hsiang-He Lee, 7000 East Avenue, Livermore, CA, 94550, U.S.A.

40 E-mail: lee1061@llnl.gov

41

42

43

1

Abstract

The presence of warm boundary layer stratiform clouds over the Eastern North Atlantic (ENA) region is commonly influenced by the Azores High, especially during the summer season. To investigate comprehensive aerosol-cloud interactions, this study employs the Weather Research and Forecast model coupled with a chemistry component (WRF-Chem), incorporating aerosol chemical components that are relevant with formation of cloud condensation nuclei (CCN) and accounting for aerosol spatiotemporal variation. This study focuses on aerosol indirect effects, particularly long-range transport aerosols, in the ENA region under three different weather regimes: ridge with surface high-pressure system, post-trough with surface high-pressure system, and weak trough. The WRF-Chem simulations conducted at a near large-eddy scale offer valuable insights into the model's performance, especially regarding its high spatial resolution in capturing the mesoscale cloud features across various weather regimes. Our result shows that introducing five times more aerosols to either non-precipitating or precipitating clouds significantly increases ambient CCN numbers, resulting in varying degrees of higher LWP. The substantial aerosol-cloud interaction especially occurs in the precipitating clouds and demonstrates the LWP susceptibility to changes in CCN under different regimes. Conversely, thin, non-rain clouds at the edges of a cloud system are prone to evaporation, exhibiting an aerosol drying effect. The aerosols released during this process transition back to the accumulation mode, facilitating future activation. This dynamic behavior is not adequately represented in prescribed-aerosol simulations.

1 Introduction

Low-level stratiform clouds are predominantly generated over oceanic regions and are categorized into three main types: warm boundary layer stratiform clouds located on the eastern side of oceanic subtropical highs, stratocumulus clouds that develop over warm western boundary currents during winter cold outbreaks, and Arctic stratus (Klein and Hartmann, 1993). Warm boundary layer stratocumulus clouds, on average, blanket around 20% of the Earth's surface annually (Wood, 2012; Warren et al., 1988). Their influence on the Earth's energy balance is substantial, primarily through their ability to reflect incoming solar radiation, resulting in significant shortwave cloud radiative effects leading to a pronounced negative net radiative effect (Chen et al., 2000; Stephens and Greenwald, 1991; Hartmann et al., 1992).

Research on aerosol-cloud interactions in warm boundary layer clouds has been ongoing since the 1970s. Twomey (1974) proposed that aerosols play an important role in influencing the Earth's energy budget by serving as cloud condensation nuclei (CCN). These CCN are crucial for cloud formation. A higher concentration of CCN results in the formation of clouds with a greater number of smaller-sized cloud droplets (Twomey, 1991). These smaller droplets enhance cloud albedo, known as the first indirect effect, and inhibit precipitation formation while prolonging cloud lifetime, known as the second indirect effect (Albrecht, 1989). In addition to these indirect effects, aerosol particles have direct, semi-direct, and indirect impacts on the atmosphere's energy budgets and surface, leading to changes in atmospheric stability (Lee et al., 2008). Until now, our understanding of aerosol-cloud interactions remains incomplete. In a recent review paper, Feingold et al. (2024) highlighted that the response of cloud amount (including liquid water content, spatial coverage, and cloud persistence) to aerosol perturbations is still unclear. Both positive and negative adjustments in liquid water path (LWP) and cloud fraction (CF) have been

86   observed. Increases in cloud amount (positive adjustments) are linked to rain suppression, whereas

87   enhanced evaporation of smaller droplets and entrainment feedback tend to decrease cloud amount

88   (negative adjustments).

89   This study focuses on warm boundary layer stratiform clouds located on the eastern side

90   of oceanic subtropical highs, specifically targeting the area over the Eastern North Atlantic (ENA)

91   region, where the U.S. Department of Energy (DOE) Atmospheric Radiation Measurement (ARM)

92   program developed a ground-based user facility in the Azores archipelago (Mather and Voyles,

93   2013). Long-term ground-based observations at the ARM ENA site, aircraft field campaigns near

94   the Azores islands, and satellite retrievals over the ENA region provide comprehensive datasets

95   for observational studies on aerosol-cloud interactions (Zheng et al., 2022; Zheng et al., 2023;

96   Ghate et al., 2023; Qiu et al., 2024).

97   The presence of stratocumulus clouds over the ENA region is commonly influenced by the

98   Azores High, also known as the Bermuda-Azores High (Rémillard and Tselioudis, 2015). This

99   semi-permanent high-pressure system typically develops over the subtropical North Atlantic

100   Ocean. The Azores High often brings stable and relatively dry conditions to the region, which can

101   contribute to the formation and maintenance of stratocumulus clouds. During the summer season,

102   the Azores High tends to strengthen and expand, leading to more persistent high-pressure

103   conditions and often warmer, drier weather in its vicinity. Although synoptic intrusions from high

104   latitudes are less frequent in the summer compared to the winter season (Wood et al., 2015), the

105   ENA region still experiences synoptic variability from weak troughs during the summer months

106   (Mechem et al., 2018; Zheng et al., 2024).

107   Leveraging the marine boundary layer cloud observations from the ARM ENA

108 observatory, this study aims to study aerosol indirect effects (AIE), especially long-range transport

109 aerosols, in the warm boundary layer clouds over the ENA region under three different synoptic

110 regimes: ridge with surface high-pressure system, post-trough with surface high-pressure system,

111 and weak trough (Mechem et al., 2018; Zheng et al., 2024). These regimes are chosen because the

112 ARM site experiences northerly wind conditions during the passage of troughs. This minimizes

113 the influence of the island effect on the observations (Ghate and Cadeddu, 2019; Zheng and Miller,

114 2022).

115   Only a few numerical studies examined aerosol-cloud interactions in marine boundary

116 layer clouds over this region (Zhang et al., 2021; Wang et al., 2020; Kazemirad and Miller, 2020;

117 Christensen et al., 2024). Wang et al. (2020), for example, used the Weather Research and Forecast

118 (WRF) model with prescribed CCN profiles to simulate perturbed long-range transport aerosol

119 concentration for two different cases of marine boundary layer (MBL) clouds. They concluded

120 that when long-range transport aerosol plumes penetrate down into the drizzling cloud deck, the

121 simulations show an increase in marine cloud fractions with larger water content, supporting a

122 positive cloud amount adjustment to CCN perturbations. Christensen et al. (2024) utilized an

123 advanced WRF configuration integrated with a Lagrangian framework to assess the effects of

124 aerosols on developing cloud fields across 10 case study days during the ENA field campaign and

125 got the same conclusion. However, a limitation of these studies is that they do not account for

126 aerosol composition acting as CCN or the changes in aerosol populations following the cloud

127 evaporation process, even though aerosol wet removal is included in their simulations.

128   To further investigate the impacts of realistic aerosol chemical components and aerosol

129 spatiotemporal variation on the AIE, this study adopts the WRF model coupled with a chemistry

130   component (WRF-Chem) to examine the AIE in the ENA region across different synoptic regimes.

131   A brief description of observational data and the WRF-Chem model, as well as the configuration

132   and numerical experiments, are given in Section 2. Simulated results are discussed in Section 3,

133   including model evaluation, model sensitivity tests, and cloud susceptibilities. The discussion and

134   summary are provided in Section 4.

135   2   Methodology

136   2.1   Observational data

137   2.1.1   MERRA-2

138   The Modern-Era Retrospective analysis for Research and Applications, Version 2

139   (MERRA-2), represents the latest advancement in global atmospheric reanalysis during the

140   satellite era. Produced by NASA's Global Modeling and Assimilation Office (GMAO), it utilizes

141   the Goddard Earth Observing System Model (GEOS) version 5.12.4 (Molod et al., 2015). The

142   aerosol species are from the dataset, inst3_3d_aer_Nv, which is an instantaneous 3-dimensional 3-

143   hourly data collection in MERRA-2 (Modeling and Office, 2015). The dataset comprises

144   assimilations of aerosol mixing ratio parameters at a native resolution of 0.5° latitude x 0.625°

145   longitude across 72 model layers, encompassing dust, sea salt, sulfur dioxide (SO_2), sulfate (SO_4),

146   black carbon (BC), and organic carbon (OC). The data is provided every three hours, beginning

147   at 00:00 UTC. Based on Wang et al. (2020), we also adopt MERRA-2 to drive the WRF-Chem

148   initial and boundary conditions for this study (see Section 2.2.2 for details).

149   2.1.2   Geostationary satellite retrievals (Meteosat)

150   Cloud properties are derived from the Spinning Enhanced Visible and Infrared Imager

151   (SEVIRI) on Meteosat-10 and Meteosat-11, which offer a spatial resolution of 3 km at nadir and

152 a half-hourly temporal resolution over the ENA region. These SEVIRI cloud products are

153 generated using the Satellite ClOud and Radiation Property retrieval System (SatCORPS)

154 algorithms (Painemal et al., 2021). These methods, developed by the Clouds and Earth's Radiant

155 Energy System (CERES) project, are specifically tailored to support ARM ground-based

156 observation sites (Minnis et al., 2011; Minnis et al., 2021). Specifically, this study adopts cloud

157 fraction for all clouds as the observational reference over the ENA region. The adopted data have

158 been specifically processed (e.g., solar zenith angle, cloud optical thickness, and cloud labels) and

159 averaged to 25 km × 25 km (Qiu et al., 2024).

160 ### 2.1.3 Aircraft observation

161 The U.S. DOE ARM Aerosol and Cloud Experiments in the Eastern North Atlantic (ACE-

162 ENA) aircraft field campaign near the Azores islands provided extensive observations of the

163 vertical distributions of aerosol and cloud properties (Wang et al., 2022). Intensive operational

164 periods (IOPs) of the ACE-ENA took place in late June and July 2017, as well as January to

165 February 2018. During the 2017 summer IOP, the ARM Aerial Facility's (AAF) Gulfstream-159

166 (G-1) aircraft delivered precise measurements of aerosol size distribution, total aerosol number

167 concentration, and chemical constituents both below and above cloud layers. SO_4 and OC mass

168 concentrations were measured using the Aerodyne High-Resolution Time-of-Flight Aerosol Mass

169 Spectrometer (HR-ToF-AMS), while refractory BC was measured by the Single Particle Soot

170 Photometer (SP2). Detailed information about each instrument is available on the ARM website

171 (https://www.arm.gov/research/campaigns/aaf2017ace-ena). In this study, aircraft measurements

172 of SO_4, OC, and BC from 19 July 2017, are utilized to assess the simulated aerosol vertical profile.

173 However, uncertainties arising from the measurements and spatiotemporal sampling strategies

174 may hinder direct comparisons of absolute values between the observations and modeled results.

2.1.4 ARM ground-based observations

The DOE ARM ground-based instruments deployed on Graciosa Island in the Azores archipelago provide comprehensive measurement of aerosols, clouds, radiation, atmospheric boundary layer, and other atmospheric properties. In this study, LWP is retrieved from the brightness temperature measured by the microwave radiometer (MWR) at 23.8 and 31.4 GHz (Liljegren et al., 2001) and used for model evaluation. The temperature and moisture profiles are from the interpolated sonde data, derived from the radiosonde measurement.

2.2 The model

2.2.1 WRF-Chem

The Weather Research and Forecasting (WRF) model version 4.4.2 (Skamarock et al., 2021) coupled with a chemistry component (WRF-Chem) (Grell et al., 2005) is used in this study. The standard WRF-Chem permits the simulation of the combined direct, indirect, and semi-direct effects of aerosols (Grell et al., 2005; Fast et al., 2006; Chapman et al., 2009). WRF-Chem version 4.4.2 has sophisticated packages to represent chemistry processes (i.e., gas-phase reaction, gas-to-particle conversion, coagulation, etc.) and aerosol size and composition (Binkowski and Shankar, 1995). In this study, the Regional Acid Deposition Model version 2 (RADM2) photochemical mechanism (Stockwell et al., 1997) is integrated alongside the Modal Aerosol Dynamics Model for Europe (MADE) and the Secondary Organic Aerosol Model (SORGAM) (Ackermann et al., 1998; Schell et al., 2001) to simulate atmospheric chemistry and the evolution of anthropogenic aerosols. MADE/SORGAM adopts a modal approach to represent the aerosol size distribution, predicting mass and number concentrations across three aerosol modes (Aiken, accumulation, and coarse). MADE/SORGAM has inorganic, organic, and secondary organic aerosols and contain aerosol formation processes including nucleation, condensation, and coagulation. WRF-Chem

198   tracks the number of particles and the mass of chemical compounds (e.g., SO_4^{2-}, NH_4^+, NO_3^-, Na^+,

199   Cl^- etc.) in each aerosol mode, including both interstitial aerosols and aerosols present in liquid

200   water (the sum of cloud and rain), as prognostic variables.

201   The size, composition, and mixing state of aerosols significantly influence their capability

202   to activate as CCN (Zaveri et al., 2010). A physically based aerosol activation parameterization

203   scheme has been developed for climate models to simulate CCN concentration accurately and

204   efficiently (Abdul-Razzak and Ghan, 2000). This aerosol activation parameterization was initially

205   designed for a single aerosol type with a lognormal size distribution. Then, they expanded this

206   parameterization to accommodate multiple externally mixed lognormal modes, with each mode

207   consisting of both soluble and insoluble materials internally mixed. However, WRF-Chem

208   (MADE/SORGAM) chemistry package adopts this global internal mixing assumption, where all

209   particles within a log-normal mode within the same grid cell are instantly combined, resulting in

210   the same chemical composition. This instantaneous internal mixing assumption modifies the

211   optical and chemical characteristics of particles in WRF-Chem simulations, potentially impacting

212   aerosol-cloud interactions, such as aerosol activation as CCN (Zhang et al., 2014).

213   2.2.2 The configuration

214   Our focus in this study is to examine aerosol-cloud interactions close to the scale of large-

215   eddy simulation (LES) over the ARM ENA site. We use WRF-Chem with a full chemistry

216   package involving sophisticated gaseous and aqueous chemical processing calculations and dry

217   and wet depositions. The numerical simulations are employed with 4 domains consisting of 4

218   horizontal resolutions of 5 km, 1.67 km, 0.56 km, and 0.19 km, respectively (Fig. 1), with one-

219   way nesting. There are 550×530 grids for D1, 451×430 grids for D2, 553×532 grids for D3,

220   and 553×532 grids for D4. The domain size of domain 4 is about 1 degree which is similar to

221 the spacing resolution of global climate models. Seventy-five vertically staggered layers are

222 stretched to have a higher resolution near the surface based on a terrain-following pressure

223 coordinate system. With this setup, the model has roughly 24 model layers in the boundary layer

224 (~2000 m). The time step is 30 and 10 seconds for advection and physics calculation for domains

225 1 and 2, respectively. The nesting inner domains 3 and 4 have the time step of 3 seconds and 1

226 second, respectively. The physics schemes adopted in the simulations are listed in Table 1. The

227 initial and boundary meteorological conditions are taken from ERA5, developed by the Copernicus

228 Climate Change Service (C3S) at ECMWF (European Centre for Medium-Range Weather), stands

229 as the fifth generation of ECMWF atmospheric reanalysis, spanning from January 1940 to the

230 present day (Hersbach et al., 2023). This comprehensive dataset offers hourly estimates of

231 numerous atmospheric, land, and oceanic climate variables, covering the entirety of Earth on a 31

232 km grid. The atmospheric component is resolved using 137 levels, spanning from the surface up

233 to 80 km in height.

234   The computational expense of conducting a 4-domain WRF-Chem simulation, particularly

235 with LES resolution, is exceedingly high. To mitigate this, we execute WRF solely for the two

236 outer domains (d01 and d02), leveraging the WRF downscaling module (ndown) (Skamarock et

237 al., 2008) to generate meteorological initial and boundary conditions for domain 3. As a result,

238 we only need to perform WRF-Chem simulations for the two inner domains (d03 and d04), leading

239 to an almost 50% reduction in total computational costs (compared to the original 4-domain run,

240 which had a throughput of 4 hours per day using 1080 cores). It is important to note that a high

241 temporal frequency for domain 3 boundary conditions is essential due to its fine horizontal

242 resolution (0.56 km). In this context, we update the boundary condition every 5 minutes for

243 domain 3.

244   To enhance the realism of aerosol mass simulation in remote marine regions, such as the

245   ENA site, we account for major aerosol species (BC, OC, and SO_4), as well as SO_2, from MERRA-

246   2 into the boundary conditions of domain 3. Aerosols in the initial condition are introduced into

247   the restart file (wrfrst) following a one-hour initial run, rather than in the initial condition file

248   (wrfinput), to address certain numerical challenges. According to the emission setup for

249   MADE/SORGAM, we assume that the Aiken mode and the accumulation mode account for 20%

250   and 80% of the aerosol mass (BC and OC), respectively (Tuccella et al., 2012). Conversely, for

251   SO_4, 80% is allocated to the Aiken mode and 20% to the accumulation mode, reflecting the faster

252   growth rate of SO_4 and a longer duration of growth from the domain 3 boundary. Because

253   MERRA-2 only provides aerosol mass, the aerosol number concentrations for different aerosol

254   species are estimated with the density assumption of BC (1.7 g cm^{-3}), OC (1.0 g cm^{-3}) and SO_4

255   (1.77 g cm^{-3}) based on Liu et al. (2012). Aerosol optical depth retrieved from satellite remote

256   sensing can offer valuable information for comparison; however, it may be subject to high bias in

257   our study cases due to cloud cover.

258   It is common to consider that the ENA region is an unpolluted area because it is far away

259   from the anthropogenic pollution sources. Besides long-range transport aerosols, two local aerosol

260   sources, dimethyl sulfide (DMS) and sea salts, are also important for the aerosol budget. Kazil et

261   al. (2011) pointed that the observed DMS flux from the ocean in the VOCALS-REx field campaign

262   over the Southeast Pacific can support a nucleation source of aerosol. DMS oxidation by nitrate

263   (NO_3) produces SO_2 and then increases SO_4 concentration (Toon et al., 1987). Since we adapted

264   SO_2 and SO_4 concentration from MERRA-2 in the initial and boundary conditions, we did not

265   double count DMS emissions in our simulations. As a result, chemical species emissions, except

266   for sea salt, are excluded from the simulations. The emission of sea salt particles is parameterized

267   using the method outlined by Clarke et al. (2006) in WRF-Chem. Sea salt emissions are driven by

268   surface wind speed. The simulated surface wind speed aligns closely with ERA-5 data; however,

269   the sea salt concentration is only one-third of the value found in the MERRA-2 analysis. To

270   improve the alignment with the sea salt aerosol concentration observed in the MERRA-2

271   reanalysis, we adjust the parameter factor for sea salt emissions to three times the original estimate

272   (further comparison can be found in Section 3).

2.3 Study cases and numerical experiment design

274   We select three specific study cases to assess the impact of long-range transport aerosols on

275   warm boundary layer clouds, with each case representing a typical meteorological regime observed

276   over the ENA site. The first case, dated 1 July 2016, exhibits the formation of overcast

277   stratocumulus clouds (Fig. 2a) within a meteorological regime characterized by a ridge system in

278   the free troposphere and a high-pressure system near the surface (Fig. 2d). Predominant

279   northwesterly and northerly winds in the area of the ARM ENA site coincide with the presence of

280   long-range transport aerosols, commonly found along the periphery of the high surface pressure

281   system (Logan et al., 2014; Gallo et al., 2023).

282   The second case on 19 July 2017 is a stratocumulus cloud case (Fig. 2b) within a post-

283   trough regime featuring a high surface pressure under the influence of a trough system (Fig. 2e).

284   Following the trough passage, robust northwesterly winds facilitated the influx of long-range

285   transport aerosols into the region, which then shifted to northerly winds as the trough moved away.

286   Because the ACE-ENA aircraft field campaign intensive operations period (IOP) was during this

287   time, aircraft aerosol observational data can be used to evaluate the model performance for this

288   case.

289   Finally, the third case, dated 23 August 2019, occurred during a period of weak trough

290   activity (Fig. 2f). Here, we noted the presence of broken, thicker stratocumulus clouds, often

291   accompanied by deeper cloud formations (Fig. 2c). Long-range transport aerosols were again

292   observed, primarily carried by northwesterly and northerly winds, albeit with weaker surface wind

293   speeds compared to the preceding two cases.

294   All simulations start at 12 UTC on the preceding day of the study case, spanning a duration

295   of 36 hours, with the initial 12 hours dedicated to spin-up. Again, aerosols in the initial condition

296   are introduced into the restart file after one-hour initial run (i.e., 13 UTC). The three

297   aforementioned cases, labeled as control cases (20160701_control, 20170719_control, and

298   20190823_control), are utilized to examine the behavior of warm boundary layer clouds under

299   diverse meteorological conditions. Additionally, we formulated three perturbed cases

300   (20160701_perturbed, 20170719_perturbed, and 20190823_perturbed) by amplifying aerosol

301   concentrations in both initial and boundary conditions, as well as sea salt emissions, by a factor of

302   five relative to each control case. These control cases represent clean conditions, with near-surface

303   CCN concentrations below 100 cm^{-3} at the ARM ENA site. A comparison between the control

304   and perturbed cases elucidates the sensitivity of warm boundary layer clouds to aerosol

305   enhancements under varying meteorological conditions, thereby contributing to a deeper

306   understanding of cloud microphysics processes under varying atmospheric dynamics.

3 Results

3.1 Model evaluation

3.1.1 Meteorological conditions

310   Figures 2g, 2h, and 2i display the model-simulated LWP in the control runs over domain 3

311   and 4. The modeled LWP is calculated in-cloud LWP only. The simulations with fine spatial

312   resolution effectively capture synoptic frontal systems and cloud features, particularly when

313   compared to the cloud images from the Meteosat satellite (Figs. 2a, 2b, and 2c). Thin, uniform

314   stratocumulus clouds on 1 July 2016 are simulated in 20160701_control, while the solid

315   stratocumulus and frontal system on 19 July 2017 are also well captured in 20170719_control.

316   Broken stratocumulus clouds on 23 August 2019 are reproduced in the simulation of

317   20190823_control. Figures 2j, 2k, and 2l display the model-simulated LWP in the perturbed runs.

318   The overcast stratocumulus clouds are simulated better in 20160701_perturbed (Fig. 2j), which

319   more accurately reflects reality.

320   The control runs serve as a basis for comparing the boundary layer structure against the

321   interpolated soundings obtained from the ARM ENA site. Figure 3 depicts the comparison,

322   showing the simulated air temperature aligning closely with the observed values. However, on 1

323   July 2016, the model (20160701_control) displays a warm bias in capturing the temperature

324   inversion (Figs. 3a and 3b), with the simulated inversion layer situated approximately 200-300 m

325   lower than observed during the whole study period. Potential temperature and relative humidity

326   have consistent performance as illustrated in Figs. S1b and S2b, respectively. While the model

327   indicates high relative humidity (> 90%) within 1000 m, observations show this extending up to

328   ~1200 m.

329   For the 19 July 2017 case, the model (20170719_control) successfully represents the

330   diurnal cycle of temperature vertical gradient within 1000 m height. However, compared to

331   observations, the model does not catch the inversion at 1500 m height near the noon time and

332   shows a warm bias in the model's simulated temperature (Figs. 3c and 3d). The model simulation

333   also tends to depict drier conditions in the evening compared to the observation (Figs. S3c and

334   S3d).

335   On 23 August 2019, characterized by a weak trough regime and higher boundary layer

336   height, the simulation of 20190823_control accurately captures warm and moist air advection in

337   the morning but has difficulty in maintaining fidelity in the late afternoon. Notably, the lower

338   troposphere becomes excessively warm and dry after 17 Z local time compared to observations

339   (Figs. 3e, 3f, S2e, S2f, S3e, and S3f).

340   In general, all simulations effectively capture large-scale conditions and cloud features

341   (Fig. 2) across different synoptic regimes but do not accurately represent temperature inversions

342   and air advection patterns. Discrepancies are noted in the simulated boundary layer height, which

343   is lower, and the inversion is weaker than actual observations. Furthermore, the discrepancies tend

344   to increase in the later stage of simulation.

345   3.1.2 Aerosol evolution

346   As mentioned in Section 2.2.2, we incorporate major aerosol species (BC, OC, and SO_4),

347   from MERRA-2 into the domain 3 initial (in the restart file at 13 UTC) and boundary conditions

348   to enhance the realism of aerosol simulation. Figure 4 shows time-series SO_4 vertical profiles

349   from both MERRA-2 and WRF-Chem for three study cases. Here, we demonstrate the time

350   evolution of SO_4. This species is the main aerosol component among the three introduced aerosol

351   species, about 60~80% of total aerosol mass, in the initial conditions.

352   Compared to the MERRA-2 data, 20160701_control well captures the long-range transport

353   SO_4 between 1000 m and 2000 m, which is above the cloud deck, on 1 July 2016 (Figs. 4a and 4b).

354   The observed high BC and OC are also concentrated in this layer (Figs. S4a and S5a), as well as

355   simulated ones (Figs. S4b and S5b). Figures 4c and 4e show two MERRA-2 time-series vertical

356   distributions of SO_4 on 19 July 2017 and 23 August 2019, both showing low-altitude (below 1500

357   m) aerosol plumes. On 19 July 2017, the concentrations of BC and OC showed two peaks – one

15

358 near the surface and another above 1500 m in the free troposphere (Figs. S4c and S5c). This

359 pattern indicates the presence of a biomass-burning signature in the plume on that day (Wang et

360 al., 2020). While the simulation of 20170719_control did not capture the near surface BC, OC,

361 and SO_4 concentration after 11 Z local time on 19 July 2017 (Figs. S4d, S5d, and 4d). It is because

362 in the case of the post-tough regime, the wind direction changes from northwesterly to northerly

363 when the trough moved away, and the aerosol plume in domain 3 did not propagate into domain 4

364 when the wind direction changed (figure not shown). However, the simulation of

365 20170719_control still captures the BC and OC plumes in the free troposphere (above 2000 m

366 height) (Figs. S4d and S5d).

367   Aircraft observations during ACE-ENA provide more accurate depictions of aerosol

368 vertical distribution and aerosol layer heights, with differentiation of aerosol type. Figure 5a shows

369 the vertical distribution of aerosol mass concentrations averaged over the flights on 19 July 2017.

370 BC, OC and SO_4 all increase with height above clouds (~1000 m), indicating downward

371 propagation of aerosol plumes and possible interaction with MBL clouds (600 – 1000 m). Here,

372 we also see that high SO_4 in the free troposphere, similar to MERRA-2, but the model

373 underestimates the OC concentration in the free troposphere. On the other hand, within the MBL,

374 there is a much higher concentration of SO_4 in the MBL than those of BC and OC in the

375 observations. This phenomenon is also captured by the WRF-Chem simulation (Fig. 5b), but the

376 model did not capture the magnitude of the SO_4 concentration.

377   Similarly, for the case of 20190823, within the low boundary layer, there is a much higher

378 concentration of SO_4 in the low boundary layer (Fig. 4e). After the noon time on 23 August 2019,

379 BC and OC show both high-altitude plumes and low-altitude plumes approaching into the domain,

380 which indicate potentially two different aerosol sources (Figs. S4e and S5e). Again, while the

381   simulation of 20190823_control well captures the time evolution of aerosol plume, the boundary

382   of high-altitude plumes and low-altitude plumes appears 300 m lower in the simulations (~600 m

383   in altitude; Figs. S4f and S5f) compared to the observations (~900 m in altitude).

384   Sea salt particles serve as an important source of CCN over the ocean, particularly in

385   unpolluted conditions. However, due to their larger particle size, sea salt particles tend to

386   accumulate near the ocean surface and are swiftly removed by dry deposition and sedimentation

387   processes (Chin et al., 2002). The simulation of 20160701_control (Figs. S6a and S6b) accurately

388   reproduces sea salt concentrations, both in magnitude and vertical distribution, consistent with

389   observations, same as the case of 20170719 (Figs. S6c and S6d). Nevertheless, the model

390   encounters difficulties in simulating sea salt concentrations for the case of 23 August 2019 (Figs.

391   S5e and S5f), corresponding to a weak-trough system (Fig. 2c). Although the simulated surface

392   wind speed matches well with ERA-5 (Fig. S7), the underestimation of sea salt concentrations may

393   be attributed to limitations in the emission parameterization, which is overly reliant on surface

394   wind speed (Gong, 2003).

395   3.1.3 Cloud properties

396   In Fig. 6, we observe a comparison between the simulated results and observations of LWP

397   and CF at different spatial scales (4 km- and domain-average, respectively) to leverage the

398   spatiotemporal advantages offered by both sets of observations. The ARM ground-based

399   instrument recorded an LWP of over 400 g m^{-2} during the nighttime with drizzle droplets reaching

400   to the surface on 1 July 2016 (Fig. 6a). As the sunrise (around 6 Z local time), the LWP decreases

401   to a range of about 100 g m^{-2} and then increases again to 600 g m^{-2} after 21 Z local time.

402   To compare with the ARM ground-based observations, the WRF-Chem simulated result is

403   averaged over 20 × 20 grids centered on the Azores, which corresponds to an approximate

404   resolution of 4 km (Fig. 6a). Overall, the control run generates a thin cloud layer with an

405   underestimated LWP during the nighttime, capturing only 10-20% of the observed LWP. The

406   simulated clouds are more consistent with the observations during the daytime, especially in the

407   perturbed run. However, it is important to note that the LWP retrieved by MWR experiences

408   significant uncertainties during drizzling or precipitating conditions. This is primarily due to the

409   scattering effects of large raindrops and raindrops accumulating on the instrument's radome, which

410   can result in an overestimation of LWP (Tian et al., 2019; Cadeddu et al., 2020).

411   Figure 6b depicts the comparison of CF between observations and WRF-Chem. The CF

412   values obtained from Meteosat are close to 1, indicating a solid cloud field. In contrast, the CF

413   simulated by 20160701_control range between 0.5 and 0.9 on a domain-averaged scale. Similar

414   to the LWP results, the simulated CFs from 20160701_control exhibit a diurnal cycle, with higher

415   values during the nighttime and lower values during the daytime. Due to the thinner clouds

416   simulated in 20160701_control based on LWP, the modeled CF is 40-60% lower than the

417   observation in the afternoon, indicating that clouds dissipate more quickly in the control run.

418   Conversely, the 20160701_perturbed scenario demonstrates improved performance in both LWP

419   and CF. This indicates that the 20160701 case is sensitive to aerosol variations, with the CCN

420   number being too low in the control run.

421   Compared to a ridge system like the case of 20160701, the WRF-Chem model has

422   difficulty in capturing the warm boundary layer clouds under a regime characterized by a post-

423   trough system (20170719) or a weak trough system (20190823). Compared to the observations,

424   the simulated LWP in 20170719_control is about 30% of the observed value (Fig. 6c. In contrast,

18

425   the simulated CF performs better, reaching about 75% of the observed value (Fig. 6d). The

426   discrepancy between the modeled results and observations may arise from delayed moisture

427   transfer from the outer domain or insufficient vertical resolution. In this instance, the cloud

428   systems move quickly under the post-trough weather regime. A 5-minute moisture input from the

429   boundary condition using WRF downscaling (ndown) may not be sufficient to transport moisture

430   into the inner domain, making it difficult for the model to develop thicker marine stratocumulus

431   clouds, especially for such high spacing resolution. On the other hand, in another ongoing project,

432   we increased the vertical layers to 99, which doubles vertical layers below 2km. However, the test

433   with 99 levels only slightly improves the cloud cover and LWP. The estimated LWP susceptibility

434   shows little to no change. The insignificant improvement indicates even higher resolution is

435   needed to fully simulate the cloud processes near the sharp boundary layer inversion for these solid

436   stratocumulus cloud layer. Another possible reason is that the 6th Order Horizontal Diffusion used

437   in the study (diff_6th_opt = 2) rapidly dissipates marine stratiform clouds, especially in the high

438   spacing resolution (Knievel et al., 2007). It is worth noting that Christensen et al. (2024) conducted

439   sensitivity tests using various shallow cumulus and microphysics schemes, and the different

440   combinations of these schemes had a substantial impact on the simulated cloud amount as well.

441   Moving to the case of 20190823, overall, compared to the observations, the control run

442   captures LWP and CF slightly better, especially in the domain-averaged scale (Figs. 6e and 6f).

443   Based on the LWP observed from ARM, there are two systems passing in the area, one between 5

444   Z to 13 Z local time and the other between 17 Z to 22 Z local time on 23 August 2019 (high ARM

445   LWP in Fig. 6e). The simulation of 20190823_control captures the first system, but slightly

446   underestimates LWP; however, the model misses the second system. The model simulated CFs

447 also match well with Meteosat (Fig. 6f). Only after 17 Z, the model misses catching the second

448 system. The CFs drops 50 – 70 % compared to the observations.

449   The underestimation of LWP and CF in model simulations leads to insufficient longwave

450 cooling at the cloud top. This reduced cooling weakens cloud-top entrainment, resulting in a less

451 pronounced boundary layer inversion and a shallower boundary layer height identified in Section

452 3.1.1. This creates a negative feedback loop, where the initial inaccuracies in cloud properties

453 affect boundary layer dynamics (Zheng et al., 2021). On the other hand, in the perturbed runs, the

454 results show an adjustment in the amounts of LWP and CF, aligning more closely with the

455 observations. This suggests that the CCN number is underestimated in the control runs (more

456 discussion in Section 3.3). The model's response to aerosol changes highlights its capability for

457 studying aerosol-cloud interactions.

458   3.2 Aerosol composition and activation

459   The advantage of utilizing WRF-Chem to investigate aerosol-cloud interactions stems from

460 its capability to simulate the spatiotemporal distribution of CCN. This modeling is based on

461 various aerosol components and their sizes, as well as their dynamic responses to wet removal

462 processes associated with clouds and precipitation. In traditional simulations that rely on fixed or

463 prescribed aerosol distributions, accurately representing these factors can be particularly

464 challenging. WRF-Chem, however, allows for a more nuanced understanding by dynamically

465 modeling how aerosol populations evolve over time, especially after cloud evaporation processes.

466 During the evaporation process, the reduction in cloud water can lead to a re-entrainment of

467 aerosols back into the atmosphere, altering their concentration and properties. This change can

468 affect subsequent cloud formation and precipitation patterns, highlighting the importance of

469 capturing these interactions for reliable predictions.

470   In this section, we concentrate on aerosol activation, considering its size and chemical

471   composition across three different cases. The following section will discuss the aerosol indirect

472   effect and how changes in cloud properties feedback into the aerosol population and its activation

473   capability.

474   In Fig. 7a, the blue solid line and blue dashed line represent the vertical profiles of total

475   aerosol number concentration (including Aiken mode and accumulation mode) and aerosol number

476   concentration of the Aiken mode, respectively. These profiles are averaged over domain 4 on 1

477   July 2016. The environment shown in the figure is characterized as clean, with a total aerosol

478   number concentration below the cloud top (approximately 1000 m in height) measuring less than

479   300 cm^{-3}. In the 20160701_control simulation, the total aerosol number is low, and approximately

480   70% of the total aerosol numbers belong to the Aiken mode. According to the study conducted by

481   Mccoy et al. (2024), which utilized aerosol number concentration measurements from ARM

482   airborne observations on 15 July 2017, it was found that the ratio of the Aiken mode to the total

483   aerosol number was approximately 50-60% within an altitude of 1000 m. Compared to this

484   observational analysis, our simulations generate an overabundance of small-sized aerosols, which

485   result in a low concentration of CCN. This discrepancy arises from the assumptions made when

486   constructing the aerosol initial and boundary conditions (80% for Aiken mode and 20% for

487   accumulation mode SO$_4$).

488   The CCN calculation presented in Fig. 7a is based on the Köhler theory, which considers

489   both the aerosol size (curvature effect) and the chemical composition (solution effect) to estimate

490   the theoretical CCN number concentration at different supersaturations. Below 1.0%

491   supersaturation, the CCN number concentration is found to be 42% of the total number of aerosol

492   number (could be estimated from 100% of accumulation mode and 16% of Aiken mode) (Fig.

493   S8a). In the simulation of 20160701_control, the CCN number concentration below 0.2% (0.5%)

494   supersaturation is only 11% (25%) of the total aerosol number, which is lower than the

495   observations reported in Wang et al. (2020), where the observed CCN number concentration under

496   0.35% supersaturation was approximately 25% of the total aerosol number. Even though SO_4 is

497   the dominant chemical component, accounting for nearly 50% (as shown in Figs. 8b and 8c), the

498   presence of an excessive number of Aiken mode aerosols may be the primary reason for the low

499   activation rate. The curvature effect caused by these Aiken mode aerosols hinders their ability to

500   act as CCN effectively.

501   In the simulation of 20170719_control, most aerosols are concentrated within a height of

502   1000 m, which corresponds to the cloud layer height (Fig. 7d). The average aerosol number

503   concentration across the entire domain is measured to be 1286 cm^{-3} within a height of 2000 m and

504   the Aiken mode is 80% of the total aerosol number in this case. The chemical composition of

505   aerosols in the 20170719_control mainly is SO_4 with the other species exhibiting lower

506   concentrations (Figs. 7e and 7f). This variation in vertical distribution leads to more aerosols being

507   activated under the cloud top at a height of 1500 m. This is attributed to the presence of a peak

508   value of accumulation mode aerosols and SO_4 at this height.

509   Because of the high number concentration of simulated Aiken mode aerosols, overall, the

510   activation rate is low. Below 1.0% supersaturation, the CCN number concentration is estimated

511   to be 25% of the total aerosol number. This could be a result of 100% of the accumulation mode

512   aerosols and 7% of the Aiken mode aerosols contributing to the CCN population (Fig. S8c). The

513   CCN number concentration below 0.2% (0.5%) supersaturation is only 4% (12%) of the total

514   aerosol number.

515   Among the three cases studied, the case of 20190823 stands out as the most polluted case,

516   but the aerosol component and vertical distribution are close to the case of 20170719 (Figs. 7c and

517   7i). The average aerosol number concentration across the entire domain is measured to be 1850

518   cm^{-3} within a height of 2000 m. The Aiken mode aerosols are also high and contribute to more

519   than 75% of the total aerosol number in this case (Figs. 7g and S8e). The large SO_4 species

520   concentration also leads to more aerosols being activated under the cloud top at a height of 2000

521   m. The CCN number concentration below 0.2% (0.5%) supersaturation is only 6% (17%) of the

522   total aerosol number, slightly better than the case of 20170719.

523   The cloud droplet numbers observed in the three cases fall within the range of CCN

524   numbers below 0.1% and 0.2% supersaturation. Therefore, in the subsequent sections, we utilize

525   the CCN number concentration below 0.2% supersaturation as a representative of the CCN

526   activation rate.

527 3.3 Cloud responses to aerosol perturbations

528   Figure 8 illustrates the comparison of time series profiles of cloud water content (CWC)

529   and CCN number concentration below 0.2% supersaturation between the control runs and

530   perturbed runs. This figure also demonstrates the CCN spatiotemporal variation in our

531   simulations. Specifically, for the case of 20160701, it is evident that the CWC in

532   20160701_perturbed exhibits a positive response to increased CCN compared to the CWC in

533   20160701_control. This result aligns with most WRF studies that use fixed or prescribed CCN

534   numbers to investigate aerosol-cloud interactions (Wang et al., 2020; Christensen et al., 2024).

535   Echoing the insufficient longwave cooling at the cloud top due to the underestimation of

536   LWP and CF in model simulations discussed in Section 3.1.3, Terai et al. (2014) also observed

537   weak cloud-top entrainment in their study of five pockets of open cells, using aircraft data from

538   the VOCALS Regional Experiment (VOCALS-REx). Their research indicated that clouds tend to

539   break up easily in the absence of aerosols, characteristic of a pristine environment. Consistent

540   with their findings, our study demonstrates that in-cloud collision–coalescence processes

541   effectively remove aerosols, particularly because of the wider range of cloud droplet sizes present

542   in a clean environment (i.e., the control runs) (Table 2). Even in the control run for 20160701, our

543   results indicate that broken open cell clouds in a pristine environment struggle to develop into

544   closed clouds.

545   Figure 9a depicts the time series of domain-averaged LWP, encompassing both cloud and

546   rain, and CCN number concentration below 0.2% supersaturation for both the 20160701_control

547   and 20160701_perturbed cases. This visualization provides a quantitative representation of the

548   change in CCN number concentration, which increases from a mean value of 32.52 cm^{-3} in the

549   control run to 127.68 cm^{-3} in the perturbed run, approximately four times higher than the control

550   run. Because we want to avoid counting high CCN number concentration above cloud top which

551   do not readily become cloud droplets, the CCN number concentration is averaged from the surface

552   up to the height of 1000 m (Wang et al., 2020).

553   The LWP in the 20160701_control case exhibits a domain mean value of 64.88 $g\ m^{-2}$,

554   which subsequently increases to 123.27 $g\ m^{-2}$ in the 20160701_perturbed case. As mentioned in

555   Section 3.1, the LWP for the 20160701 case follows a diurnal cycle, with higher values during

556   nighttime and lower values during daytime. This diurnal cycle is also observed in the perturbed

557   simulation, with the larger differences in CCN and LWP between the control run and perturbed

558   run during nighttime (Fig. 9a).

559   After increasing the aerosol concentration, the cloud droplet number in the

560   20160701_perturbed run demonstrates similar responses. In the 20160701_control case, the

561   domain mean value of the cloud droplet number is 14.03 cm^{-3}, which subsequently increases to

562   45.52 cm^{-3} in the 20160701_perturbed case. As the cloud droplet number increases, the cloud

563   radius decreases from 12.23 μm in the control run to 10.08 μm in the perturbed case.

564   The case of 20170719 represents a post-trough weather regime, and Fig. 8c illustrates the

565   passage of a frontal system in the area after 8 Z local time on that day. In the 20170719_perturbed

566   simulation, the CWC increases following the system's passage (Fig. 8d) compared to the CWC in

567   the 20170719_control run. Additionally, the ambient CCN number in the perturbed run is also

568   higher. The time variation of CCN concentration in Fig. 9c shows elevated CCN numbers before

569   and after the system enters the domain. In the 20170719_control case, the domain mean value of

570   CCN number concentration is 60.51 cm^{-3}, which subsequently increases to 253.51 cm^{-3} in the

571   20170719_perturbed case. The domain-averaged LWP also exhibits an increase, rising from 59.31

572   g m^{-2} in the 20170719_control run to 74.07 g m^{-2} in the 20170719_perturbed case. Notably, this

573   change primarily occurs after the passage of the frontal system.

574   The cloud droplet number consistently shows higher values in the perturbed case (Fig. 9d),

575   and this pattern is similar to the difference in CCN between the two runs of 20170719 (Fig. 9c).

576   In the 20170719_control case, the domain mean value of cloud droplet number is 20.70 cm^{-3}, while

577   the value is 56.09 cm^{-3} in the perturbed case. When the cloud droplet number increases in the

578   perturbed run, the cloud radius decreases from 9.90 μm in the control run to 7.49 μm in the

579   perturbed case. This reduction in cloud radius is even smaller than the cloud radius observed in

580   the case of 20160701.

581   The case of 20190823 is similar to the case of 20170719, but it represents a weak trough

582   weather regime. Figure 8e also illustrates the passage of a cloud system in the area between 5 Z

583   to 17 Z local time on 23 August 2019, and the CWC in the perturbed run increases during this

584   period. Quantitatively, in the 20190823_control case, the domain mean value of CCN number

585   concentration is 124.32 cm^{-3}, which subsequently increases to 475.37 cm^{-3} in the

586   20190823_perturbed case, which is also about three times higher. The domain-averaged LWP

587   also exhibits an increase, rising from 48.92 g m^{-2} in the 20190823_control run to 58.53 g m^{-2} in

588   the 20190823_perturbed case.

589   Differing from the case of 20170719, the frontal system moved away from the study

590   domain after the noontime, the differences of CCN number or cloud droplet number between the

591   control and perturbed runs becomes even more pronounced after the system (Figs. 9e and 9f). It

592   is because aerosols are transported to the area following the frontal system (Fig. 4f) which in turn

593   activates more aerosols as CCN. In the 20190823_control case, the domain mean value of cloud

594   droplet number is 33.94 cm^{-3}, while the value is 79.97 cm^{-3} in the perturbed case. When the cloud

595   droplet number increases in the perturbed run, the cloud radius decreases from 8.51 μm in the

596   control run to 6.45 μm in the perturbed case. This reduction in cloud radius is similar to the cloud

597   radius observed in the case of 20170719.

598   We observe that large aerosol-induced LWP occurs during the periods of rainfall (Fig. S9).

599   To accurately quantify the differences, we calculate the average LWP over approximately 25 km

600   of domain 4. This results in 16 averaged grids per output file, with each file generated every 10

601   minutes. This averaging process is based on Arola et al. (2022) and Zhou and Feingold (2023) to

602   avoid the impact of heterogeneity and co-variability on the results. Specifically, we aggregate the

26

603   simulation grids with a spacing resolution of approximately 190 m to form a larger grid of around

604   25 km for each 10-minute simulation output, as shown in Fig. S10a.

605   Table 2 presents the 10-minute mean and standard deviation of several variables, including

606   CCN, LWP, cloud droplet number (Nc), cloud radius (Re), and rainfall intensity (RI), across three

607   study cases. The classification of "rain" and "non-rain" is based on the RI (unit: mm hr^{-1}) on the

608   averaged grid. Specifically, a grid is considered as "rain" if the RI is greater than zero. In the

609   control cases, the averaged CCN number is 73.07 cm^{-3}, and the corresponding LWP is 53.17 g m^{-}

610   ^{2}. However, in the perturbed cases, the CCN number increases approximately threefold, reaching

611   218.21 cm^{-3}, and the LWP increases by 49% to 79.25 g m^{-2}. The introduction of additional aerosols

612   in the perturbed cases also leads to a significant increase in the Nc number, from 22.68 cm^{-3} in the

613   control cases to 59.74 cm^{-3} in the perturbed cases. Consequently, the Re decreases by 21% from

614   9.97 μm to 7.83 μm, and the RI decreases by 11% from 0.009 mm hr^{-1} to 0.008 mm hr^{-1}.

615   To investigate the interaction between aerosols and clouds, we analyze the results

616   separately for rain and non-rain grids. In both the control and perturbed cases, we observe that the

617   CCN number within 1000 m is lower in the rain grids compared to the non-rain grids, primarily

618   due to the washout effect caused by rainfall. Additionally, the LWP over the rain grids is generally

619   higher than that over the non-rain grids. Furthermore, when comparing the control and perturbed

620   cases, we find that the LWP over the rain grids increases by 57% from 58.57 g m^{-2} to 91.81 g m^{-2}.

621   In contrast, the LWP over the non-rain grids only increases by 28% (Table 2). This difference can

622   be attributed to the conversion of cloud droplets to raindrops through processes like autoconversion

623   and collection, which occurs more prominently over the rain grids. We also observe that in the

624   non-rain grids, especially at the cloud edges (or low LWP), the perturbed cases reveal an increased

625   presence of small cloud droplets. This abundance of smaller droplets facilitates evaporation,

626   resulting in a reduced LWP (e.g., clouds in the bottom right corner of Figs. S10a and S10b).

627   Consequently, Nc over the rain grids is lower compared to Nc over the non-rain grids. Moreover,

628   when introducing aerosols in the perturbed runs, the results over the rain grids exhibit larger cloud

629   drops and a wider radius spectrum compared to the results over the non-rain grids. This suggests

630   that the presence of aerosols has a more pronounced effect on cloud properties within the rain

631   grids.

632   Zheng et al. (2022) conducted a study on the aerosol-cloud interaction using ground-based

633   measurements from the ARM program, focusing on the influence of environmental variables.

634   Their findings revealed that when there is ample water vapor and low CCN loading, the active

635   coalescence process leads to a broader size distribution of cloud droplets, resulting in an increase

636   in cloud droplet radius. On the other hand, when there is enhanced activation of CCN and

637   condensational growth of cloud droplets due to higher CCN loading below the cloud, the cloud

638   droplet radius decreases. This combined effect signifies an intensified aerosol-cloud interaction,

639   leading to a broad range of cloud droplet radii. The simulated results in our study, specifically

640   over the rain grids where a sufficient water vapor environment is considered, demonstrate a

641   significant aerosol-cloud interaction, where increased CCN introduces more newly converted

642   droplets, resulting in a broad range of cloud droplet radii.

643   Since we utilize a comprehensive aerosol module in WRF-Chem to examine aerosol-cloud

644   interactions, we are able to explore how changes in cloud properties, driven by increased CCN,

645   affect aerosol concentrations. For example, in the post-trough regime (20170917 case) and the

646   weak trough regime (20190823 case), we observe that the cloud structure exhibits more open-cell

647   stratocumulus clouds (Figs. 2h and 2i). As mentioned above, the increased number of smaller

648   cloud droplets at the cloud edge facilitate evaporation and results in a lower LWP (Fig. S10). The

649   larger aerosols from the evaporated clouds return to the accumulation mode, making them more

650   likely to activate as CCN again.

651   To demonstrate how robust this process on the ACI, we calculate the time series of the

652   ratio of the number concentration of CCN at a supersaturation of 0.2% in the perturbed runs to that

653   in the control runs, normalized by the corresponding accumulation mode aerosol concentration,

654   defined as $\left.(CCN_{0.2\%}/Accu.\,aerosols)_{perturbed}\middle/(CCN_{0.2\%}/Accu.\,aerosols)_{control}\right.$, shown in

655   Fig. 10. A ratio greater than 1 suggests that accumulation mode aerosols in the perturbed cases

656   are more readily activated as CCN at a supersaturation of 0.2%, especially in the cases of 20170719

657   and 20190823. Conversely, a ratio less than 1 is observed during the first half of the day in the

658   20160701 case, which is attributed to the very low levels of accumulation mode aerosols in the

659   model.

3.4 Cloud liquid water path (LWP) susceptibilities

661   In this study, the susceptibility of LWP to changes in CCN concentration is quantified

662   using the logarithmic slope between LWP and CCN, denoted as $dln(LWP)/dln(CCN)$

663   (Gryspeerdt et al., 2019). This slope represents the sensitivity of the LWP in warm stratocumulus

664   clouds to variations in CCN concentration, like shown in Fig. S10c. As presented in Table 2, we

665   aggregate the simulation grids with a spacing resolution of approximately 190 m to form a larger

666   grid of around 25 km for each 10-minute simulation output. This averaging process helps to reduce

667   the impact of heterogeneity and co-variability on the results.

668   Figure 11 illustrates the averaged cloud susceptibilities for various LWP and CCN or Nc

669   bins across three study periods. The logarithmic slope between LWP and CCN is calculated at

670   each output time (every 10 minutes) using data from 16 aggregated grid points from the control

671 run and 16 aggregated grid points from the perturbed run. Our study reveals that when the CCN

672 concentration is below 100 cm^{-3}, the susceptibility for different LWP and CCN values is positive

673 and the values are large, indicating that changes in LWP are sensitive to variations in CCN number.

674 Here also demonstrates the AIE is large when an increase in CCN can have a large impact on LWP

675 enhancement. However, when the mean CCN concentration exceeds 100 cm^{-3}, the relationship

676 between LWP and CCN becomes more complex, with both positive and negative susceptibilities

677 observed. This suggests that the change in LWP is influenced by other factors, such as

678 environmental conditions and cloud precipitation status. (as shown in Fig. 11a). Over 70% of the

679 results meet the criterion of statistical significance ($p \leq 0.01$), further supporting the robustness of

680 the observed relationships. It is important to note that the CCN number used in our study is

681 averaged from the surface up to the height of 1000 m, which may introduce uncertainty to the

682 absolute values of susceptibility by including aerosols that are not directly involved in the aerosol-

683 cloud interaction (Wang et al., 2020).

684 Additionally, our simulations indicate that the Nc in this study is generally low, with a

685 mean value typically below 80 cm^{-3}. For different LWP and Nc values, the susceptibility is mostly

686 positive, indicating that changes in LWP are sensitive to variations in Nc number (as shown in Fig.

687 11c).

688 When we investigate the variation of LWP susceptibility over time, we observe that

689 positive susceptibilities for different LWP and CCN (Nc) typically occur during periods of no rain

690 or light rain (Figs. 12 and S9). On 1 July 2016, the time series of LWP susceptibility for different

691 CCN or Nc shows a diurnal cycle, with large positive values during the nighttime and small

692 positive values in the afternoon. During heavy rain events, such as from 8 to 15 Z local time on

693 19 July 2017 and from 23 Z to 14 Z on 23 August 2019 (Fig. S9), the LWP susceptibilities are

694   negative or close to zero (Figs. 12c and 12e). In the perturbed cases, during the heavy rainfall

695   periods, some aggregated grids show very low LWP (Fig. S10c). This reduction in LWP is caused

696   by the evaporation from small cloud droplets at non-rain grids on the cloud edge. Those low LWP

697   grids in the perturbed runs result in a negative or near-zero logarithmic slope between LWP and

698   CCN (Figs. S10c, 12c and 12e), although the domain mean LWP is higher in the perturbed case

699   than in the control case (Figs. 9c and 9e).

700   To further illustrate the reduction in LWP due to evaporation at the cloud edge, Fig. 13

701   presents the relative change in $ln(LWP)$ between the perturbed and control cases across different

702   LWP percentile ranges in the control case during the periods of negative LWP susceptibility, as

703   shown in Fig. 12. The results indicate a decrease in LWP in the perturbed cases compared to the

704   control cases for pixels with the lowest LWP percentile range (0-25%). We assume that this range

705   corresponds to thin clouds at the edges of the cloud cover.

706   Figures 11b and 11d display the mean Re susceptibilities for different CCN number and

707   Nc, respectively. The results consistently show that as CCN number or Nc increases, the radius

708   of the cloud droplets decreases. Additionally, the change in Re is more pronounced when Nc (or

709   CCN number) is higher.

710   In this study, the logarithmic slope between LWP and CCN in the LWP susceptibility

711   calculation is based on a linear assumption. Hoffmann et al. (2024) introduced a heuristic model

712   that represents a significant advancement in understanding the process-level adjustments of cloud

713   water in stratocumulus clouds, suggesting that the relationship may resemble a reversed "V" shape.

714   Figure 13 indicates that the decrease in LWP (negative susceptibilities) in the perturbed cases

715   occurs only in low LWP clouds (thin and non-rain clouds). Conversely, LWP increases (positive

716   susceptibilities) in thicker, precipitating clouds under the perturbed scenarios, which is consistent

717   with the findings of Hoffmann et al. (2024). Since our study aggregates grids to a 25 km resolution,

718   we are able to capture such spatial heterogeneity and retrieve a negative susceptibility due to the

719   evaporation of thin clouds at cloud edge while at 100-km scale (domain-averaged shown in Figs.

720   S11 and S12), the signal is dominated by the increase of LWP at cloud core. However, based on

721   the current study cases, we may not have sufficient data samples to illustrate a relationship beyond

722   the linear assumption.

4   Discussion and summary

724   This study focuses on aerosol indirect effects (AIE), particularly involving long-range

725   transport aerosols, in the Eastern North Atlantic (ENA) region. It specifically examines these

726   effects on warm boundary layer stratiform clouds located on the eastern side of oceanic subtropical

727   highs under three different weather regimes: a ridge with a surface high-pressure system, a post-

728   trough with a surface high-pressure system, and a weak trough. We select three specific case

729   studies (i.e., 20160701, 20170719, and 20190823) to assess the impact of long-range transport

730   aerosols on warm boundary layer clouds, with each case representing a typical meteorological

731   regime observed over the ENA site.

732   To investigate aerosol-cloud interactions more realistically, incorporating aerosol

733   chemistry components that activate to cloud condensation nuclei (CCN) and accounting for aerosol

734   spatiotemporal variation, this study employs the Weather Research and Forecast model coupled

735   with a chemistry component (WRF-Chem). This approach provides a detailed examination of AIE

736   in the ENA region under the three specified weather regimes. We employ a downscaling technique

737   to conduct WRF-Chem simulations for the two inner domains (with the outer domains utilizing

738   WRF). This approach results in nearly a 50% reduction in total computational costs, achieving a

739   throughput of 8 hours per day using 1,080 cores.

740   We incorporate major aerosol species (BC, OC, and SO_4), as well as SO_2, from MERRA-

741   2 to provide aerosol initial and boundary conditions, labeled as control cases. Additionally, we

742   formulate three perturbed cases by amplifying aerosol concentrations in both initial and boundary

743   conditions, as well as sea salt emissions, by a factor of five relative to each control case. Since

744   aerosol features are primarily determined by aerosol initial and boundary conditions, a higher

745   Aiken mode assumption in the major aerosol component (i.e., SO_4) regarding the aerosol mode

746   ratio (80% for Aiken mode and 20% for accumulation mode) results in fewer aerosols activating

747   as CCN due to the curvature effect in our simulations.

748   The WRF-Chem model captures the cloud structure in the case of 20160701 but

749   underestimates the cloud amount. It simulates the formation of thin, uniform stratocumulus clouds

750   within a meteorological regime characterized by a ridge system in the free troposphere and a high-

751   pressure system near the surface. However, the cases of 20170719 and 20190823 exhibit the

752   development of thicker but broken solid stratocumulus clouds within a post-trough regime and a

753   weak trough, respectively. With the fast-moving cloud systems and strong surface wind, the WRF-

754   Chem model struggles to capture the development and movement of these cloud systems due to

755   delayed moisture transport from outer boundary condition and potential insufficient vertical

756   resolution.

757   In all cases, compared to the observations, the WRF-Chem model underestimates the liquid

758   water path (LWP) and cloud fraction due to warmer and lower simulated boundary layer. In the

759   perturbed cases, we find 57% higher aerosol-induced LWP, especially for the rain grids. We also

760   note that the perturbed cases exhibit lower rainfall intensity, indicating a rainfall suppression effect

761   attributed to high CCN concentrations as concluded in previous studies (Wang et al., 2020;

762   Christensen et al., 2024). In contrast, the LWP over the non-rain grids only increases by 28%.

33

763 Moreover, when introducing aerosols in the perturbed runs, the results over the rain grids exhibit

764 larger cloud drops and a wider radius spectrum compared to the results over the non-rain grids.

765 This suggests that the presence of aerosols has a more pronounced effect on cloud properties within

766 the rain grids. The non-rain grids over the cloud edge can have lower LWP because smaller cloud

767 droplets are easy to evaporate.

768 Our study further elucidates the intricate feedback mechanisms governing aerosol-cloud

769 interactions and aerosol properties. In both the post-trough and weak trough regimes, we observe

770 a pronounced tendency for the cloud structure to develop more open-cell stratocumulus clouds.

771 At the peripheries of these clouds, the perturbed cases demonstrate a significant increase in the

772 presence of small cloud droplets. This heightened abundance of smaller droplets promotes

773 evaporation, thereby leading to a marked reduction in LWP.

774 As these clouds evaporate, the aerosols that are released return to the accumulation mode.

775 This transition enhances their likelihood of reactivating as CCN. Consequently, this cycle

776 underscores the dynamic interplay between aerosol properties and cloud formation, highlighting

777 how changes in aerosol concentrations can influence cloud microphysics and, ultimately,

778 precipitation processes.

779 Additionally, the susceptibility of LWP to changes in CCN concentration is quantified

780 using the logarithmic slope between LWP and CCN. Our result shows when the CCN

781 concentration is low, LWP is sensitive to variations in CCN number, with higher CCN number

782 concentration leading to higher LWP. However, when the mean CCN concentration is relatively

783 high, LWP is not as sensitive to changes in CCN, the LWP susceptibilities are small in magnitude,

784 with both positive and negative values. Those negative values are caused by the evaporation from

785 small cloud droplets at non-rain grids on the cloud edge.

786   In Wang et al. (2020), the LWC susceptibility for a light precipitation case on 18 July 2017

787   also shows positive values based on three sensitivity runs with CCN concentrations of 10, 100,

788   and 1000 cm^{-3}. The cloud properties in their study are averaged over all cloud points in the

789   innermost domain. We adopt the same method as Wang et al. (2020) to estimate the LWP

790   susceptibility   using   the   domain   mean   values,   defined   as

791    $\Delta ln(LWP_{perturbed} - LWP_{control})/\Delta ln(CCN_{perturbed} - CCN_{control})$.   This   approach

792   predominantly yields positive values for LWP susceptibility across the three study cases (see Figs.

793   S11 and S12). This suggests that the 25-km resolution is able to capture such spatial heterogeneity

794   and retrieve a negative susceptibility due to the evaporation of thin clouds at cloud edge while at

795   100-km scale (domain-averaged), the signal is dominated by the increase of LWP at cloud core.

796   Conversely, the LWP susceptibilities associated with varying cloud droplet numbers

797   reported in Qiu et al. (2024) reveal significant negative values in LWP susceptibility in response

798   to high cloud droplet numbers, a trend that is partially reflected in our study. Further investigation

799   is required to reconcile the difference in LWP responses between observational data and model

800   simulations. Additionally, a more accurate estimation of LWP susceptibility to changes in CCN

801   concentration is necessary.

802   Moreover, future research will focus on addressing the identified issues within the model,

803   such as improving the representation of transported aerosol size distributions, resolving the overly

804   fragmented stratocumulus cloud layers with sharp boundary layer inversions, and comparing the

805   modeled cloud susceptibilities with observational data through simulations of ship tracks and local

806   aerosol perturbations.

807

Code and data availability:

The WRF-Chem code (v4.4.2) used in this study has been released on GitHub (https://github.com/wrf-model/WRF/releases/download/v4.4.2/v4.4.2.tar.gz). The observational data used in this study are available at https://doi.org/10.5281/zenodo.13356995. Other WRF-Chem simulated outputs for the plots in this paper are available at https://doi.org/10.5281/zenodo.13357040.

Author contributions:

H.-H. Lee and X. Zheng provided ideas and designed the experiments in this study. H.-H. Lee conducted all the simulations and analyses. H.-H. Lee leads and coordinates the manuscript with inputs from coauthors.

Competing interests.

At least one of the (co-)authors is a member of the editorial board of Atmospheric Chemistry and Physics.

Acknowledgements:

829

Reference:

831 Abdul-Razzak, H. and Ghan, S. J.: A parameterization of aerosol activation: 2. Multiple
832 aerosol types, Journal of Geophysical Research: Atmospheres, 105, 6837-6844,
833 https://doi.org/10.1029/1999JD901161, 2000.
834 Ackermann, I. J., Hass, H., Memmesheimer, M., Ebel, A., Binkowski, F. S., and Shankar, U.:
835 Modal aerosol dynamics model for Europe: development and first applications,
836 Atmospheric Environment, 32, 2981-2999, http://dx.doi.org/10.1016/S1352-
837 2310(98)00006-5, 1998.
838 Albrecht, B. A.: Aerosols, Cloud Microphysics, and Fractional Cloudiness, Science, 245,
839 1227-1230, doi:10.1126/science.245.4923.1227, 1989.
840 Arola, A., Lipponen, A., Kolmonen, P., Virtanen, T. H., Bellouin, N., Grosvenor, D. P.,
841 Gryspeerdt, E., Quaas, J., and Kokkola, H.: Aerosol effects on clouds are concealed by
842 natural cloud heterogeneity and satellite retrieval errors, Nature Communications, 13,
843 7357, 10.1038/s41467-022-34948-5, 2022.
844 Binkowski, F. S. and Shankar, U.: The Regional Particulate Matter Model: 1. Model
845 description and preliminary results, Journal of Geophysical Research: Atmospheres, 100,
846 26191-26209, https://doi.org/10.1029/95JD02093, 1995.
847 Cadeddu, M. P., Ghate, V. P., and Mech, M.: Ground-based observations of cloud and
848 drizzle liquid water path in stratocumulus clouds, Atmos. Meas. Tech., 13, 1485-1499,
849 10.5194/amt-13-1485-2020, 2020.
850 Chapman, E. G., Gustafson Jr, W. I., Easter, R. C., Barnard, J. C., Ghan, S. J., Pekour, M. S.,
851 and Fast, J. D.: Coupling aerosol-cloud-radiative processes in the WRF-Chem model:
852 Investigating the radiative impact of elevated point sources, Atmos. Chem. Phys., 9, 945-
853 964, 10.5194/acp-9-945-2009, 2009.
854 Chen, F. and Dudhia, J.: Coupling an Advanced Land Surface–Hydrology Model with the
855 Penn State–NCAR MM5 Modeling System. Part I: Model Implementation and Sensitivity,
856 Monthly Weather Review, 129, 569-585, https://doi.org/10.1175/1520-
857 0493(2001)129<0569:CAALSH>2.0.CO;2, 2001.
858 Chen, T., Rossow, W. B., and Zhang, Y.: Radiative Effects of Cloud-Type Variations, Journal
859 of Climate, 13, 264-286, 10.1175/1520-0442(2000)013<0264:Reoctv>2.0.Co;2, 2000.
860 Chin, M., Ginoux, P., Kinne, S., Torres, O., Holben, B. N., Duncan, B. N., Martin, R. V.,
861 Logan, J. A., Higurashi, A., and Nakajima, T.: Tropospheric Aerosol Optical Thickness from
862 the GOCART Model and Comparisons with Satellite and Sun Photometer Measurements,
863 Journal of the Atmospheric Sciences, 59, 461-483, https://doi.org/10.1175/1520-
864 0469(2002)059<0461:TAOTFT>2.0.CO;2, 2002.
865 Christensen, M. W., Wu, P., Varble, A. C., Xiao, H., and Fast, J. D.: Aerosol-induced closure
866 of marine cloud cells: enhanced effects in the presence of precipitation, Atmos. Chem.
867 Phys., 24, 6455-6476, 10.5194/acp-24-6455-2024, 2024.

868 Clarke, A. D., Owens, S. R., and Zhou, J.: An ultrafine sea-salt flux from breaking waves:
869 Implications for cloud condensation nuclei in the remote marine atmosphere, Journal of
870 Geophysical Research: Atmospheres, 111, https://doi.org/10.1029/2005JD006565, 2006.
871 Fast, J. D., Gustafson Jr., W. I., Easter, R. C., Zaveri, R. A., Barnard, J. C., Chapman, E. G.,
872 Grell, G. A., and Peckham, S. E.: Evolution of ozone, particulates, and aerosol direct
873 radiative forcing in the vicinity of Houston using a fully coupled meteorology-chemistry-
874 aerosol model, Journal of Geophysical Research: Atmospheres, 111,
875 https://doi.org/10.1029/2005JD006721, 2006.
876 Feingold, G., Ghate, V. P., Russell, L. M., Blossey, P., Cantrell, W., Christensen, M. W.,
877 Diamond, M. S., Gettelman, A., Glassmeier, F., Gryspeerdt, E., Haywood, J., Hoffmann, F.,
878 Kaul, C. M., Lebsock, M., McComiskey, A. C., McCoy, D. T., Ming, Y., Mülmenstädt, J.,
879 Possner, A., Prabhakaran, P., Quinn, P. K., Schmidt, K. S., Shaw, R. A., Singer, C. E.,
880 Sorooshian, A., Toll, V., Wan, J. S., Wood, R., Yang, F., Zhang, J., and Zheng, X.: Physical
881 science research needed to evaluate the viability and risks of marine cloud brightening,
882 Science Advances, 10, eadi8594, doi:10.1126/sciadv.adi8594, 2024.
883 Gallo, F., Uin, J., Sanchez, K. J., Moore, R. H., Wang, J., Wood, R., Mei, F., Flynn, C.,
884 Springston, S., Azevedo, E. B., Kuang, C., and Aiken, A. C.: Long-range transported
885 continental aerosol in the eastern North Atlantic: three multiday event regimes influence
886 cloud condensation nuclei, Atmos. Chem. Phys., 23, 4221-4246, 10.5194/acp-23-4221-
887 2023, 2023.
888 Ghate, V. P. and Cadeddu, M. P.: Drizzle and Turbulence Below Closed Cellular Marine
889 Stratocumulus Clouds, Journal of Geophysical Research: Atmospheres, 124, 5724-5737,
890 https://doi.org/10.1029/2018JD030141, 2019.
891 Ghate, V. P., Surleta, T., Magaritz-Ronen, L., Raveh-Rubin, S., Gallo, F., Carlton, A. G., and
892 Azevedo, E. B.: Drivers of Cloud Condensation Nuclei in the Eastern North Atlantic as
893 Observed at the ARM Site, Journal of Geophysical Research: Atmospheres, 128,
894 e2023JD038636, https://doi.org/10.1029/2023JD038636, 2023.
895 Gong, S. L.: A parameterization of sea-salt aerosol source function for sub- and super-
896 micron particles, Global Biogeochemical Cycles, 17,
897 https://doi.org/10.1029/2003GB002079, 2003.
898 Grell, G. A., Peckham, S. E., Schmitz, R., McKeen, S. A., Frost, G., Skamarock, W. C., and
899 Eder, B.: Fully coupled "online" chemistry within the WRF model, Atmospheric
900 Environment, 39, 6957-6975, https://doi.org/10.1016/j.atmosenv.2005.04.027, 2005.
901 Gryspeerdt, E., Goren, T., Sourdeval, O., Quaas, J., Mülmenstädt, J., Dipu, S., Unglaub, C.,
902 Gettelman, A., and Christensen, M.: Constraining the aerosol influence on cloud liquid
903 water path, Atmos. Chem. Phys., 19, 5331-5347, 10.5194/acp-19-5331-2019, 2019.
904 Hartmann, D. L., Ockert-Bell, M. E., and Michelsen, M. L.: The Effect of Cloud Type on
905 Earth's Energy Balance: Global Analysis, Journal of Climate, 5, 1281-1304, 10.1175/1520-
906 0442(1992)005<1281:Teocto>2.0.Co;2, 1992.
907 Hersbach, H., Bell, B., Berrisford, P., Biavati, G., Horányi, A., Muñoz Sabater, J., Nicolas, J.,
908 Peubey, C., Radu, R., Rozum, I., Schepers, D., Simmons, A., Soci, C., Dee, D., and Thépaut,
909 J.-N.: ERA5 hourly data on single levels from 1940 to present. Copernicus Climate Change
910 Service (C3S) Climate Data Store (CDS) [dataset], 10.24381/cds.adbb2d47 2023.

Hoffmann, F., Glassmeier, F., and Feingold, G.: The impact of aerosol on cloud water: a heuristic perspective, Atmos. Chem. Phys., 24, 13403-13412, 10.5194/acp-24-13403-2024, 2024.

Hong, S.-Y. and Jang, J.: Impacts of Shallow Convection Processes on a Simulated Boreal Summer Climatology in a Global Atmospheric Model, Asia-Pacific Journal of Atmospheric Sciences, 54, 361-370, 10.1007/s13143-018-0013-3, 2018.

Iacono, M. J., Delamere, J. S., Mlawer, E. J., Shephard, M. W., Clough, S. A., and Collins, W. D.: Radiative forcing by long-lived greenhouse gases: Calculations with the AER radiative transfer models, Journal of Geophysical Research: Atmospheres, 113, 10.1029/2008jd009944, 2008.

Janjić, Z. I.: The Step-Mountain Eta Coordinate Model: Further Developments of the Convection, Viscous Sublayer, and Turbulence Closure Schemes, Monthly Weather Review, 122, 927-945, https://doi.org/10.1175/1520-0493(1994)122<0927:TSMECM>2.0.CO;2, 1994.

kazemirad, M. and Miller, M. A.: Summertime Post-Cold-Frontal Marine Stratocumulus Transition Processes over the Eastern North Atlantic, Journal of the Atmospheric Sciences, 77, 2011-2037, https://doi.org/10.1175/JAS-D-19-0167.1, 2020.

Kazil, J., Wang, H., Feingold, G., Clarke, A. D., Snider, J. R., and Bandy, A. R.: Modeling chemical and aerosol processes in the transition from closed to open cells during VOCALS-REx, Atmos. Chem. Phys., 11, 7491-7514, 10.5194/acp-11-7491-2011, 2011.

Klein, S. A. and Hartmann, D. L.: The Seasonal Cycle of Low Stratiform Clouds, Journal of Climate, 6, 1587-1606, 10.1175/1520-0442(1993)006<1587:Tscols>2.0.Co;2, 1993.

Knievel, J. C., Bryan, G. H., and Hacker, J. P.: Explicit Numerical Diffusion in the WRF Model, Monthly Weather Review, 135, 3808-3824, https://doi.org/10.1175/2007MWR2100.1, 2007.

Lee, S. S., Donner, L. J., Phillips, V. T. J., and Ming, Y.: The dependence of aerosol effects on clouds and precipitation on cloud-system organization, shear and stability, Journal of Geophysical Research: Atmospheres, 113, https://doi.org/10.1029/2007JD009224, 2008.

Liljegren, J. C., Clothiaux, E. E., Mace, G. G., Kato, S., and Dong, X.: A new retrieval for cloud liquid water path using a ground-based microwave radiometer and measurements of cloud temperature, Journal of Geophysical Research: Atmospheres, 106, 14485-14500, https://doi.org/10.1029/2000JD900817, 2001.

Liu, X., Easter, R. C., Ghan, S. J., Zaveri, R., Rasch, P., Shi, X., Lamarque, J. F., Gettelman, A., Morrison, H., Vitt, F., Conley, A., Park, S., Neale, R., Hannay, C., Ekman, A. M. L., Hess, P., Mahowald, N., Collins, W., Iacono, M. J., Bretherton, C. S., Flanner, M. G., and Mitchell, D.: Toward a minimal representation of aerosols in climate models: description and evaluation in the Community Atmosphere Model CAM5, Geosci. Model Dev., 5, 709-739, 10.5194/gmd-5-709-2012, 2012.

Logan, T., Xi, B., and Dong, X.: Aerosol properties and their influences on marine boundary layer cloud condensation nuclei at the ARM mobile facility over the Azores, Journal of Geophysical Research: Atmospheres, 119, 4859-4872, https://doi.org/10.1002/2013JD021288, 2014.

953   Mather, J. H. and Voyles, J. W.: The Arm Climate Research Facility: A Review of Structure
954   and Capabilities, Bulletin of the American Meteorological Society, 94, 377-392,
955   https://doi.org/10.1175/BAMS-D-11-00218.1, 2013.
956   McCoy, I. L., Wyant, M. C., Blossey, P. N., Bretherton, C. S., and Wood, R.: Aitken Mode
957   Aerosols Buffer Decoupled Mid-Latitude Boundary Layer Clouds Against Precipitation
958   Depletion, Journal of Geophysical Research: Atmospheres, 129, e2023JD039572,
959   https://doi.org/10.1029/2023JD039572, 2024.
960   Mechem, D. B., Wittman, C. S., Miller, M. A., Yuter, S. E., and de Szoeke, S. P.: Joint
961   Synoptic and Cloud Variability over the Northeast Atlantic near the Azores, Journal of
962   Applied Meteorology and Climatology, 57, 1273-1290, https://doi.org/10.1175/JAMC-D-17-
963   0211.1, 2018.
964   Mellor, G. L. and Yamada, T.: Development of a turbulence closure model for geophysical
965   fluid problems, Reviews of Geophysics, 20, 851-875,
966   https://doi.org/10.1029/RG020i004p00851, 1982.
967   Minnis, P., Sun-Mack, S., Young, D. F., Heck, P. W., Garber, D. P., Chen, Y., Spangenberg,
968   D. A., Arduini, R. F., Trepte, Q. Z., Smith, W. L., Ayers, J. K., Gibson, S. C., Miller, W. F.,
969   Hong, G., Chakrapani, V., Takano, Y., Liou, K. N., Xie, Y., and Yang, P.: CERES Edition-2
970   Cloud Property Retrievals Using TRMM VIRS and Terra and Aqua MODIS Data—Part I:
971   Algorithms, IEEE Transactions on Geoscience and Remote Sensing, 49, 4374-4400,
972   10.1109/TGRS.2011.2144601, 2011.
973   Minnis, P., Sun-Mack, S., Chen, Y., Chang, F. L., Yost, C. R., Smith, W. L., Heck, P. W.,
974   Arduini, R. F., Bedka, S. T., Yi, Y., Hong, G., Jin, Z., Painemal, D., Palikonda, R., Scarino, B.
975   R., Spangenberg, D. A., Smith, R. A., Trepte, Q. Z., Yang, P., and Xie, Y.: CERES MODIS
976   Cloud Product Retrievals for Edition 4—Part I: Algorithm Changes, IEEE Transactions on
977   Geoscience and Remote Sensing, 59, 2744-2780, 10.1109/TGRS.2020.3008866, 2021.
978   Mlawer, E. J., Taubman, S. J., Brown, P. D., Iacono, M. J., and Clough, S. A.: Radiative
979   transfer for inhomogeneous atmospheres: RRTM, a validated correlated-k model for the
980   longwave, Journal of Geophysical Research: Atmospheres, 102, 16663-16682,
981   https://doi.org/10.1029/97JD00237, 1997.
982   Modeling, G. and Office, A.: MERRA-2 inst3_3d_aer_Nv: 3d, 3-hourly, instantaneous,
983   model-level, assimilation, aerosol mixing ratio V5. 12.4, 2015.
984   Molod, A., Takacs, L., Suarez, M., and Bacmeister, J.: Development of the GEOS-5
985   atmospheric general circulation model: evolution from MERRA to MERRA2, Geosci. Model
986   Dev., 8, 1339-1356, 10.5194/gmd-8-1339-2015, 2015.
987   Monin, A. S. and Obukhov, A. M.: Basic laws of turulent mixing in the atmosphere near the
988   ground, Tr. Inst. Teor. Geofiz. Akad. Nauk SSSR, 24, 1963-1987, 1954.
989   Morrison, H., Thompson, G., and Tatarskii, V.: Impact of Cloud Microphysics on the
990   Development of Trailing Stratiform Precipitation in a Simulated Squall Line: Comparison of
991   One- and Two-Moment Schemes, Monthly Weather Review, 137, 991-1007,
992   https://doi.org/10.1175/2008MWR2556.1, 2009.
993   Painemal, D., Spangenberg, D., Smith Jr, W. L., Minnis, P., Cairns, B., Moore, R. H.,
994   Crosbie, E., Robinson, C., Thornhill, K. L., Winstead, E. L., and Ziemba, L.: Evaluation of
995   satellite retrievals of liquid clouds from the GOES-13 imager and MODIS over the

996 midlatitude North Atlantic during the NAAMES campaign, Atmos. Meas. Tech., 14, 6633-
997 6646, 10.5194/amt-14-6633-2021, 2021.
998 Qiu, S., Zheng, X., Painemal, D., Terai, C. R., and Zhou, X.: Daytime variation in the aerosol
999 indirect effect for warm marine boundary layer clouds in the eastern North Atlantic, Atmos.
1000 Chem. Phys., 24, 2913-2935, 10.5194/acp-24-2913-2024, 2024.
1001 Rémillard, J. and Tselioudis, G.: Cloud Regime Variability over the Azores and Its
1002 Application to Climate Model Evaluation, Journal of Climate, 28, 9707-9720,
1003 https://doi.org/10.1175/JCLI-D-15-0066.1, 2015.
1004 Schell, B., Ackermann, I. J., Hass, H., Binkowski, F. S., and Ebel, A.: Modeling the formation
1005 of secondary organic aerosol within a comprehensive air quality model system, Journal of
1006 Geophysical Research: Atmospheres (1984–2012), 106, 28275-28293, 2001.
1007 Skamarock, W., Klemp, J., Dudhia, J., Gill, D., Liu, Z., Berner, J., and Huang, X.: A
1008 description of the advanced research WRF model version 4.3 (No. NCAR/TN-556+
1009 STR).[Software], 2021.
1010 Skamarock, W. C., Klemp, J. B., Dudhia, J., Gill, D. O., Barker, D. M., Duda, M. G., Huang,
1011 X.-Y., Wang, W., and Powers, J. G.: A description of the advanced research WRF version 3,
1012 NCAR technical note, 475, 10.5065, 2008.
1013 Stephens, G. L. and Greenwald, T. J.: The Earth's radiation budget and its relation to
1014 atmospheric hydrology: 2. Observations of cloud effects, Journal of Geophysical Research:
1015 Atmospheres, 96, 15325-15340, 10.1029/91jd00972, 1991.
1016 Stockwell, W. R., Kirchner, F., Kuhn, M., and Seefeld, S.: A new mechanism for regional
1017 atmospheric chemistry modeling, Journal of Geophysical Research: Atmospheres, 102,
1018 25847-25879, 10.1029/97JD00849, 1997.
1019 Terai, C. R., Bretherton, C. S., Wood, R., and Painter, G.: Aircraft observations of aerosol,
1020 cloud, precipitation, and boundary layer properties in pockets of open cells over the
1021 southeast Pacific, Atmos. Chem. Phys., 14, 8071-8088, 10.5194/acp-14-8071-2014, 2014.
1022 Tian, J., Dong, X., Xi, B., Williams, C. R., and Wu, P.: Estimation of liquid water path below
1023 the melting layer in stratiform precipitation systems using radar measurements during
1024 MC3E, Atmos. Meas. Tech., 12, 3743-3759, 10.5194/amt-12-3743-2019, 2019.
1025 Toon, O. B., Kasting, J. F., Turco, R. P., and Liu, M. S.: The sulfur cycle in the marine
1026 atmosphere, Journal of Geophysical Research: Atmospheres, 92, 943-963,
1027 https://doi.org/10.1029/JD092iD01p00943, 1987.
1028 Tuccella, P., Curci, G., Visconti, G., Bessagnet, B., Menut, L., and Park, R. J.: Modeling of
1029 gas and aerosol with WRF/Chem over Europe: Evaluation and sensitivity study, Journal of
1030 Geophysical Research: Atmospheres, 117, https://doi.org/10.1029/2011JD016302, 2012.
1031 Twomey, S.: Pollution and the planetary albedo, Atmospheric Environment (1967), 8, 1251-
1032 1256, https://doi.org/10.1016/0004-6981(74)90004-3, 1974.
1033 Twomey, S.: Aerosols, clouds and radiation, Atmospheric Environment. Part A. General
1034 Topics, 25, 2435-2442, https://doi.org/10.1016/0960-1686(91)90159-5, 1991.
1035 Wang, J., Wood, R., Jensen, M. P., Chiu, J. C., Liu, Y., Lamer, K., Desai, N., Giangrande, S.
1036 E., Knopf, D. A., Kollias, P., Laskin, A., Liu, X., Lu, C., Mechem, D., Mei, F., Starzec, M.,
1037 Tomlinson, J., Wang, Y., Yum, S. S., Zheng, G., Aiken, A. C., Azevedo, E. B., Blanchard, Y.,
1038 China, S., Dong, X., Gallo, F., Gao, S., Ghate, V. P., Glienke, S., Goldberger, L., Hardin, J. C.,
1039 Kuang, C., Luke, E. P., Matthews, A. A., Miller, M. A., Moffet, R., Pekour, M., Schmid, B.,

1040   Sedlacek, A. J., Shaw, R. A., Shilling, J. E., Sullivan, A., Suski, K., Veghte, D. P., Weber, R.,
1041   Wyant, M., Yeom, J., Zawadowicz, M., and Zhang, Z.: Aerosol and Cloud Experiments in the
1042   Eastern North Atlantic (ACE-ENA), Bulletin of the American Meteorological Society, 103,
1043   E619-E641, https://doi.org/10.1175/BAMS-D-19-0220.1, 2022.
1044   Wang, Y., Zheng, X., Dong, X., Xi, B., Wu, P., Logan, T., and Yung, Y. L.: Impacts of long-
1045   range transport of aerosols on marine-boundary-layer clouds in the eastern North Atlantic,
1046   Atmos. Chem. Phys., 20, 14741-14755, 10.5194/acp-20-14741-2020, 2020.
1047   Warren, S. G., Hahn, C. J., London, J., Chervin, R. M., Jenne, R. L., Colorado Univ., B., CO .
1048   Cooperative Inst. for Research in Environmental Sciences, Colorado Univ., B., CO . Dept.
1049   of Astrophysical, Planetary,, Sciences, A., and National Center for Atmospheric Research,
1050   B., CO): Global distribution of total cloud cover and cloud type amounts over the ocean,
1051   United States, Medium: ED; Size: Pages: (305 p), 10.2172/5415329, 1988.
1052   Wood, R.: Stratocumulus Clouds, Monthly Weather Review, 140, 2373-2423,
1053   10.1175/mwr-d-11-00121.1, 2012.
1054   Wood, R., Wyant, M., Bretherton, C. S., Rémillard, J., Kollias, P., Fletcher, J., Stemmler, J.,
1055   de Szoeke, S., Yuter, S., Miller, M., Mechem, D., Tselioudis, G., Chiu, J. C., Mann, J. A. L.,
1056   O'Connor, E. J., Hogan, R. J., Dong, X., Miller, M., Ghate, V., Jefferson, A., Min, Q., Minnis,
1057   P., Palikonda, R., Albrecht, B., Luke, E., Hannay, C., and Lin, Y.: Clouds, Aerosols, and
1058   Precipitation in the Marine Boundary Layer: An Arm Mobile Facility Deployment, Bulletin of
1059   the American Meteorological Society, 96, 419-440, https://doi.org/10.1175/BAMS-D-13-
1060   00180.1, 2015.
1061   Zaveri, R. A., Barnard, J. C., Easter, R. C., Riemer, N., and West, M.: Particle-resolved
1062   simulation of aerosol size, composition, mixing state, and the associated optical and cloud
1063   condensation nuclei activation properties in an evolving urban plume, Journal of
1064   Geophysical Research: Atmospheres, 115, https://doi.org/10.1029/2009JD013616, 2010.
1065   Zhang, H., DeNero, S. P., Joe, D. K., Lee, H. H., Chen, S. H., Michalakes, J., and Kleeman,
1066   M. J.: Development of a source oriented version of the WRF/Chem model and its
1067   application to the California regional PM_{10} / $PM_{2.5}$ air quality
1068   study, Atmos. Chem. Phys., 14, 485-503, 10.5194/acp-14-485-2014, 2014.
1069   Zhang, Z., Song, Q., Mechem, D. B., Larson, V. E., Wang, J., Liu, Y., Witte, M. K., Dong, X.,
1070   and Wu, P.: Vertical dependence of horizontal variation of cloud microphysics:
1071   observations from the ACE-ENA field campaign and implications for warm-rain simulation
1072   in climate models, Atmos. Chem. Phys., 21, 3103-3121, 10.5194/acp-21-3103-2021, 2021.
1073   Zheng, Q. and Miller, M. A.: Summertime Marine Boundary Layer Cloud, Thermodynamic,
1074   and Drizzle Morphology over the Eastern North Atlantic: A Four-Year Study, Journal of
1075   Climate, 35, 4805-4825, https://doi.org/10.1175/JCLI-D-21-0568.1, 2022.
1076   Zheng, X., Dong, X., Xi, B., Logan, T., and Wang, Y.: Distinctive aerosol-cloud-precipitation
1077   interactions in marine boundary layer clouds from the ACE-ENA and SOCRATES aircraft
1078   field campaigns, EGUsphere, 2023, 1-45, 10.5194/egusphere-2023-2608, 2023.
1079   Zheng, X., Xi, B., Dong, X., Wu, P., Logan, T., and Wang, Y.: Environmental effects on
1080   aerosol–cloud interaction in non-precipitating marine boundary layer (MBL) clouds over
1081   the eastern North Atlantic, Atmos. Chem. Phys., 22, 335-354, 10.5194/acp-22-335-2022,
1082   2022.

1083   Zheng, X., Qiu, S., Zhang, D., Adebiyi, A. A., Zheng, X., Faruque, O., Tao, C., and Wang, J.:
1084   Variability of Eastern North Atlantic Summertime Marine Boundary Layer Clouds and
1085   Aerosols Across Different Synoptic Regimes Identified with Multiple Conditions, ESS Open
1086   Archive, 10.22541/essoar.172434363.30466798/v1, 2024.
1087   Zheng, Y., Zhu, Y., Rosenfeld, D., and Li, Z.: Climatology of Cloud-Top Radiative Cooling in
1088   Marine Shallow Clouds, Geophysical Research Letters, 48, e2021GL094676,
1089   https://doi.org/10.1029/2021GL094676, 2021.
1090   Zhou, X. and Feingold, G.: Impacts of Mesoscale Cloud Organization on Aerosol-Induced
1091   Cloud Water Adjustment and Cloud Brightness, Geophysical Research Letters, 50,
1092   e2023GL103417, https://doi.org/10.1029/2023GL103417, 2023.

1093

1094

1095

1096

1097   Table 1. WRF physics scheme configuration
1098

Physics Processes	Scheme	Reference
Microphysics	Morrison (2 moments) scheme	Morrison et al. (2009)
Longwave radiation	RRTMG scheme	Mlawer et al. (1997)
Shortwave radiation	RRTMG scheme	Iacono et al. (2008)
Surface-layer	Monin-Obukhov surface layer	Monin and Obukhov (1954)
Land surface	Unified Noah land-surface model	Chen and Dudhia (2001)
Planetary boundary layer	MYJ (Eta) TKE scheme (d01 and d02 only)	Mellor and Yamada (1982) Janjić (1994)
Shallow cumulus parameterization	GRIMS scheme (d01 and d02 only)	Hong and Jang (2018)

1099
1100
1101

1102 Table 2. Ten-minute mean and standard deviation of cloud condensation nuclei (CCN), liquid
1103 water path (LWP), cloud droplet number (Nc), cloud radius (Re), and rainfall intensity (RI) over
1104 three study cases. Data are averaged over ~25 km of the domain 4 and total 16 averaged grids are
1105 in the domain 4. Rain and non-rain are averaged the grids when the RI on the grid is larger than
1106 and equal to zero, respectively. Only CCN are averaged within 1000 m height over the domain 4,
1107 other variables are averaged within 2000 m height.

Area	Case	CCN (cm^{-3})	LWP (g m^{-2})	Nc (cm^{-3})	Re (μm)	RI (mm hr^{-1})
Domain	Control	73.07 ± 48.77	53.17 ± 32.65	22.68 ± 11.59	9.97 ± 2.31	0.009 ± 0.033
	Perturbed	286.88 ± 183.69 (+293%)	79.25 ± 56.62 (+49%)	59.74 ± 27.29 (+163%)	7.83 ± 2.02 (-21%)	0.008 ± 0.033 (-11%)
Rain	Control	68.15 ± 48.05	58.57 ± 31.69	20.17 ± 9.33	10.47 ± 2.07	0.011 ± 0.035
	Perturbed	250.14 ± 153.23 (+267%)	91.81 ± 55.06 (+57%)	53.01 ± 20.39 (+163%)	8.35 ± 1.83 (-20%)	0.009 ± 0.036 (-18%)
Non-Rain	Control	103.73 ± 41.52	18.91 ± 9.81	38.57 ± 11.93	6.81 ± 0.76	0 ± 0
	Perturbed	444.47 ± 217.08 (+328%)	24.22 ± 15.80 (+28%)	89.24 ± 33.42 (+131%)	5.54 ± 0.90 (-19%)	0 ± 0

1108
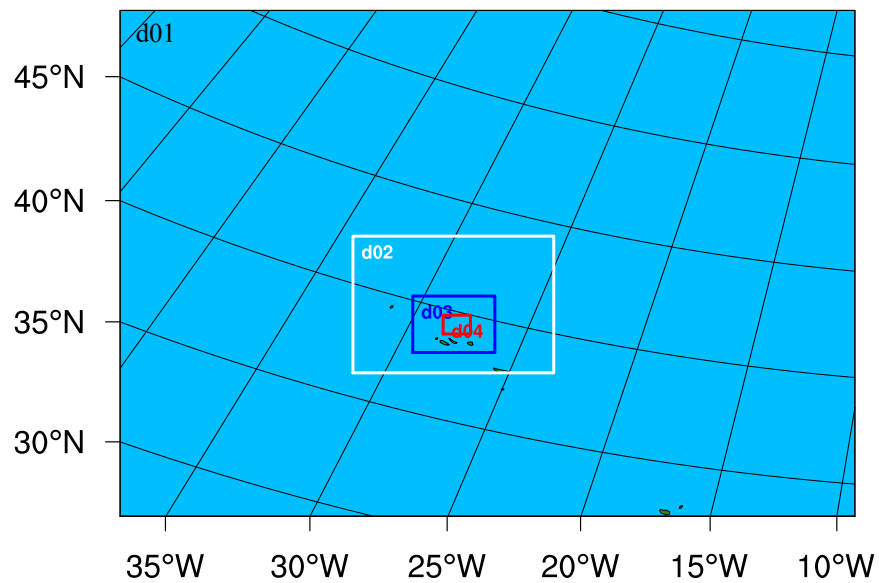
1109

1110   Figure 1. Model domains are designed for simulations. The 4 domains denote 4 horizontal
1111   resolutions of 5 km (d01), 1.67 km (d02), 0.56 km (d03), and 0.19 km (d04), respectively.

1112

1113
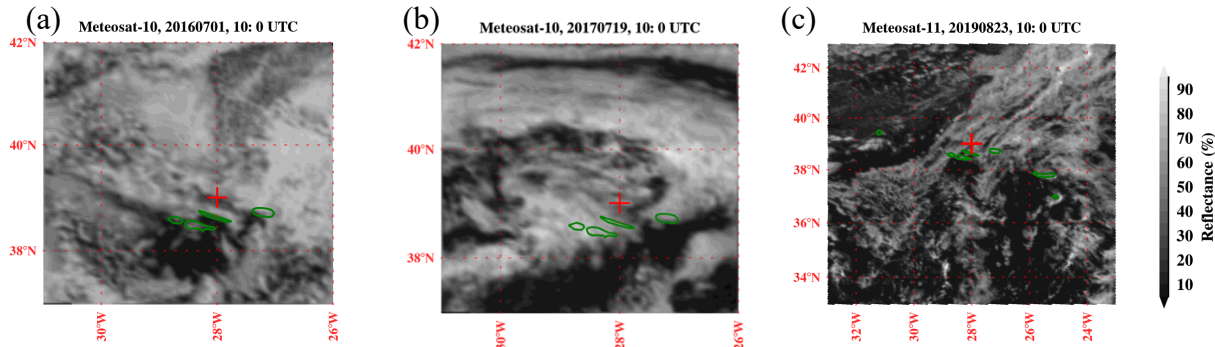
1114
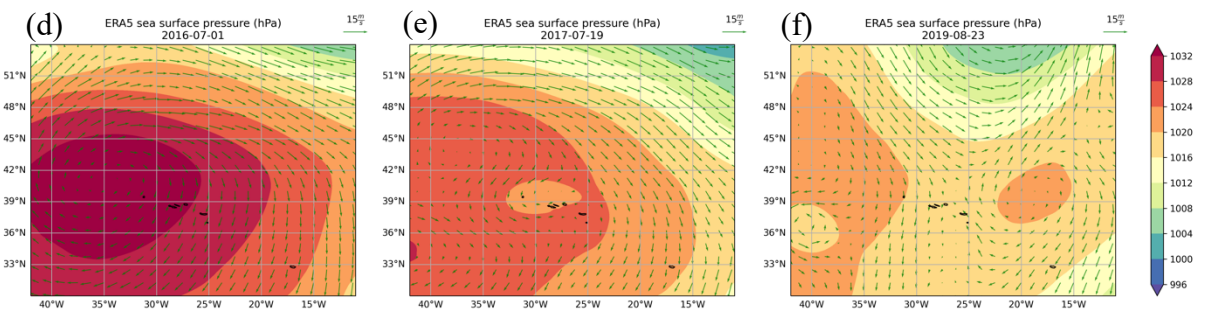
1115
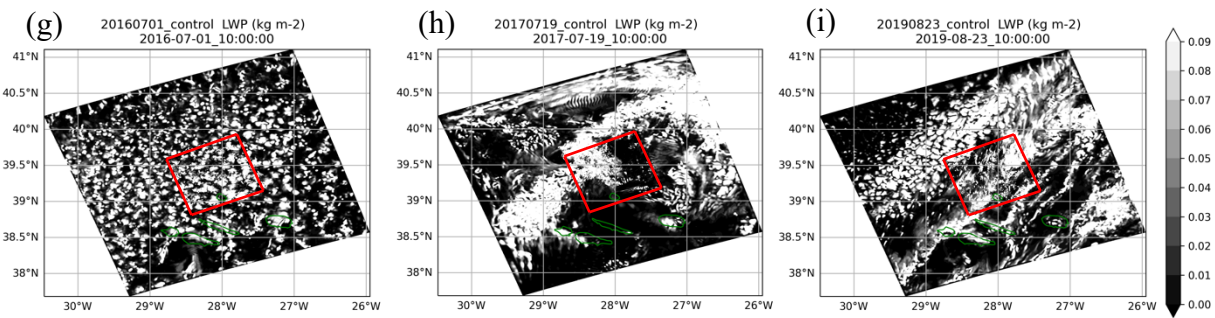
1116
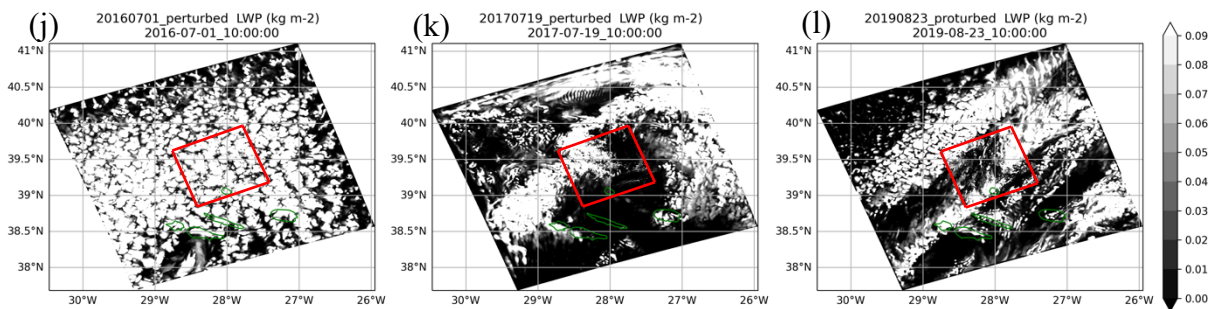
1117

Figure 2. Spinning Enhanced Visible Infra-Red Imager (SEVIRI) images from the Meteosat
satellite at 10:00 UTC on (a) 1 July 2016, (b) 19 July 2017, and (c) 23 August 2019 over the
ENA. (d), (e), and (f) are on the same day of (a), (b), and (c), respectively, but from the ERA5
mean sea surface pressure (contour; units: hPa) and 10-meter surface wind (arrow; units: m s^{-1}).
(g), (h), and (i) are on the same day of (a), (b), and (c), respectively, but from the WRF-Chem

1123   simulated liquid water path (LWP; units: kg m^{-2}) in the control runs, while (j), (k), and (l) are in

1124   the perturbed runs. The red boxes in the figures indicate the result from domain 4.

1125
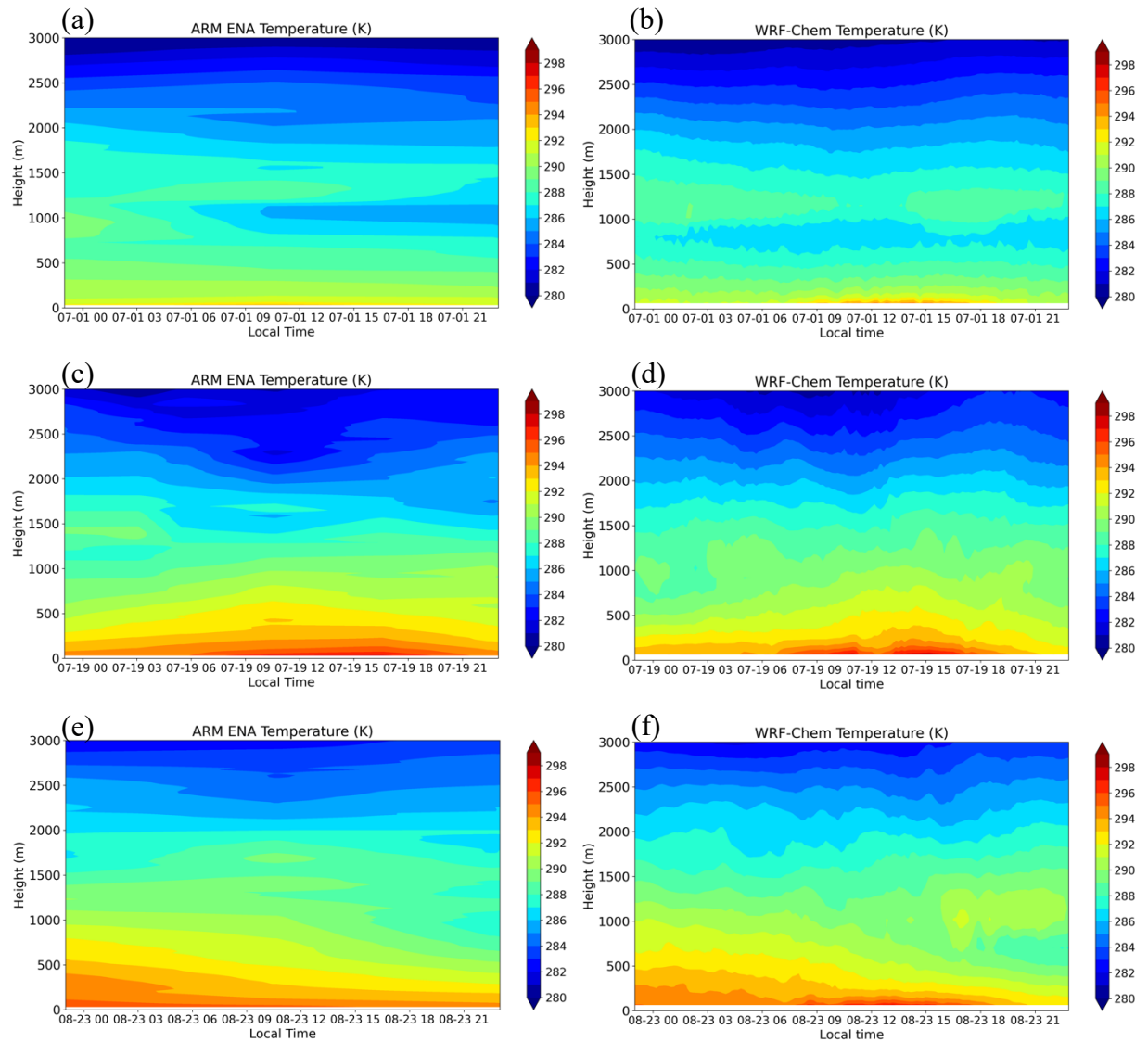
Figure 3. The time series (local time; UTC -1 hour) of temperature profiles (units: K) from ARM interpolated soundings at the Azores (39.09°N, 28.02°W) on (a) 1 July 2016, (c) 19 July 2017, and (e) 23 August 2019. Panels (b), (d), and (f) depict the same dates as (a), (c), and (e), respectively, but show the average temperature from WRF-Chem simulated results over 20 × 20 grids centered on the Azores (approximately 4 km resolution).

1136

1137

1138
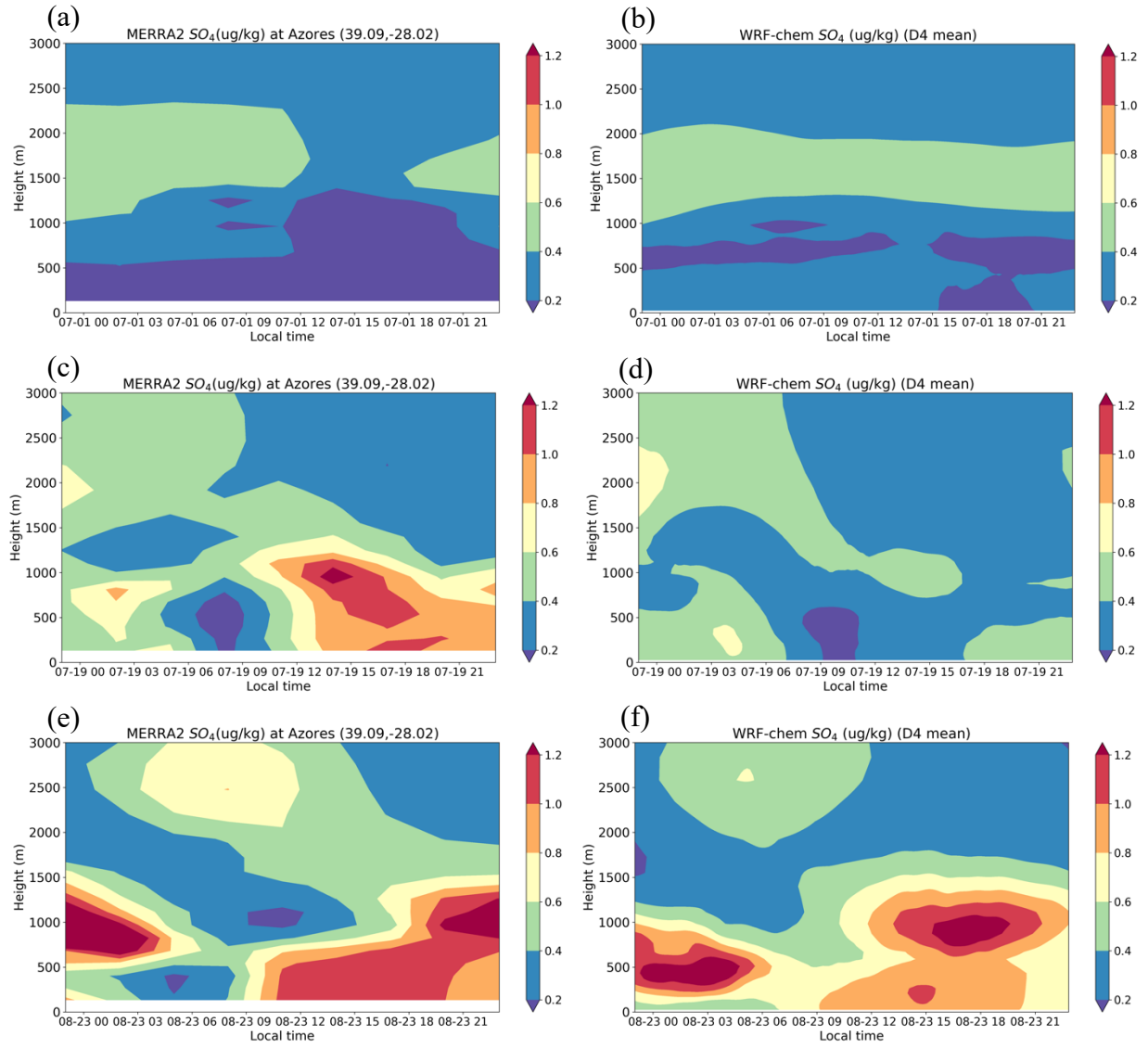
Figure 4. The time series (local time; UTC – 1 hour) of SO$_4$ profiles (units: µg kg^{-1}) from
MERRA-2 at the Azores (39.09°N, 28.02°W) on (a) 1 July 2016, (c) 19 July 2017, and (e) 23
August 2019. Panels (b), (d), and (f) depict the same dates as (a), (c), and (e), respectively, but
show the average aerosol concentration from WRF-Chem simulated data over domain 4.

1144

(a) ARM airborne-measured (20170719)
(b) WRF-chem (20170719)
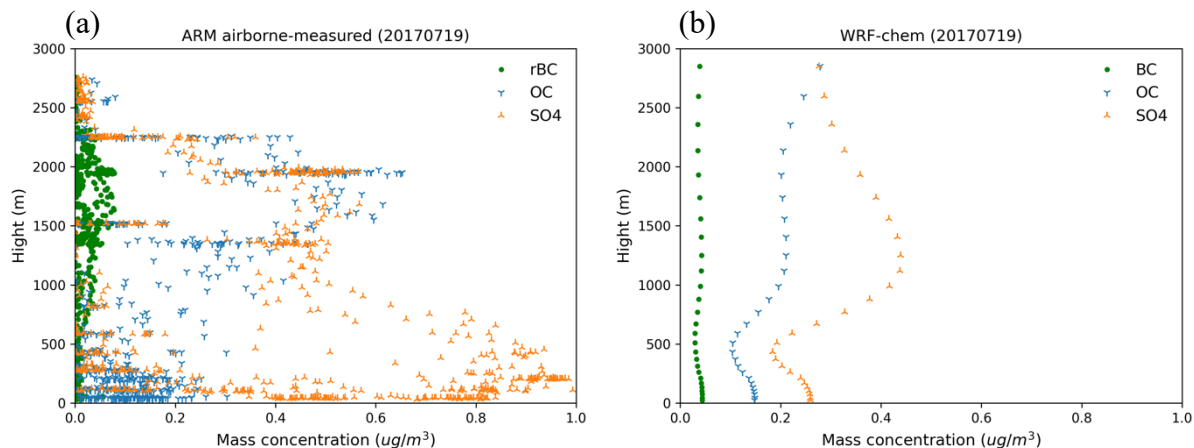
1145
1146
1147 Figure 5. (a) ARM airborne-measured vertical profiles of SO₄, OC and refractory BC (rBC) mass
1148 concentration (units: $\mu g\ cm^{-3}$) averaged over multiple flights on 19 July 2017. Note that the
1149 highly uncertain and noisy aerosol observations between 600 – 1000 m height due to cloud
1150 contamination. (b) WRF-Chem simulated vertical profile of SO₄, OC, and BC mass
1151 concentration (units: $\mu g\ cm^{-3}$) averaged over domain 4 during the flight time from 8:40 to 11:50
1152 UTC.
1153
1154
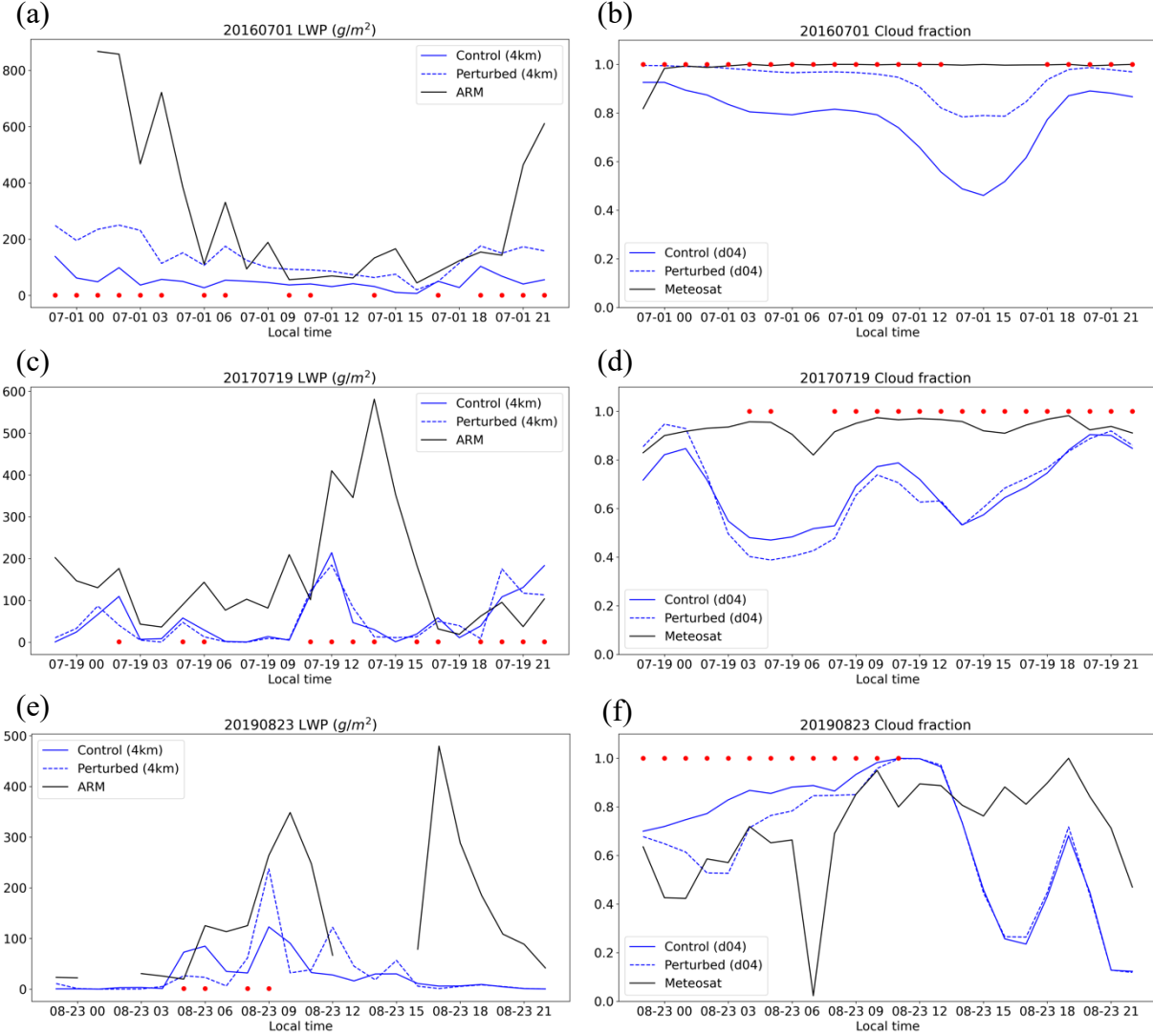
Figure 6. (a), (c), and (e) are the hourly time series (local time; UTC - 1 hour) of 4 km-averaged (4 km) liquid water path (units: g m^{-2}) simulated from WRF-Chem (blue solid line) and observed from ARM (black solid line) on 1 July 2016, 19 July 2017, and 23 August 2019, respectively. (b), (d), and (f) are the hourly time series of domain-averaged (d04) cloud fraction simulated from WRF-Chem (blue solid line) and observaed from Meteosat (black solid line) on 1 July 2016, 19 July 2017, and 23 August 2019, respectively. The 4 km-averaged data are averaged from the model simulated results over 20 × 20 grids centered on the Azores (approximately 4 km resolution). The red dots indicate when rainfall intensity is higher than 0.001 (0.01) mm hr^{-1} in 4-km averaged area (domain 4).
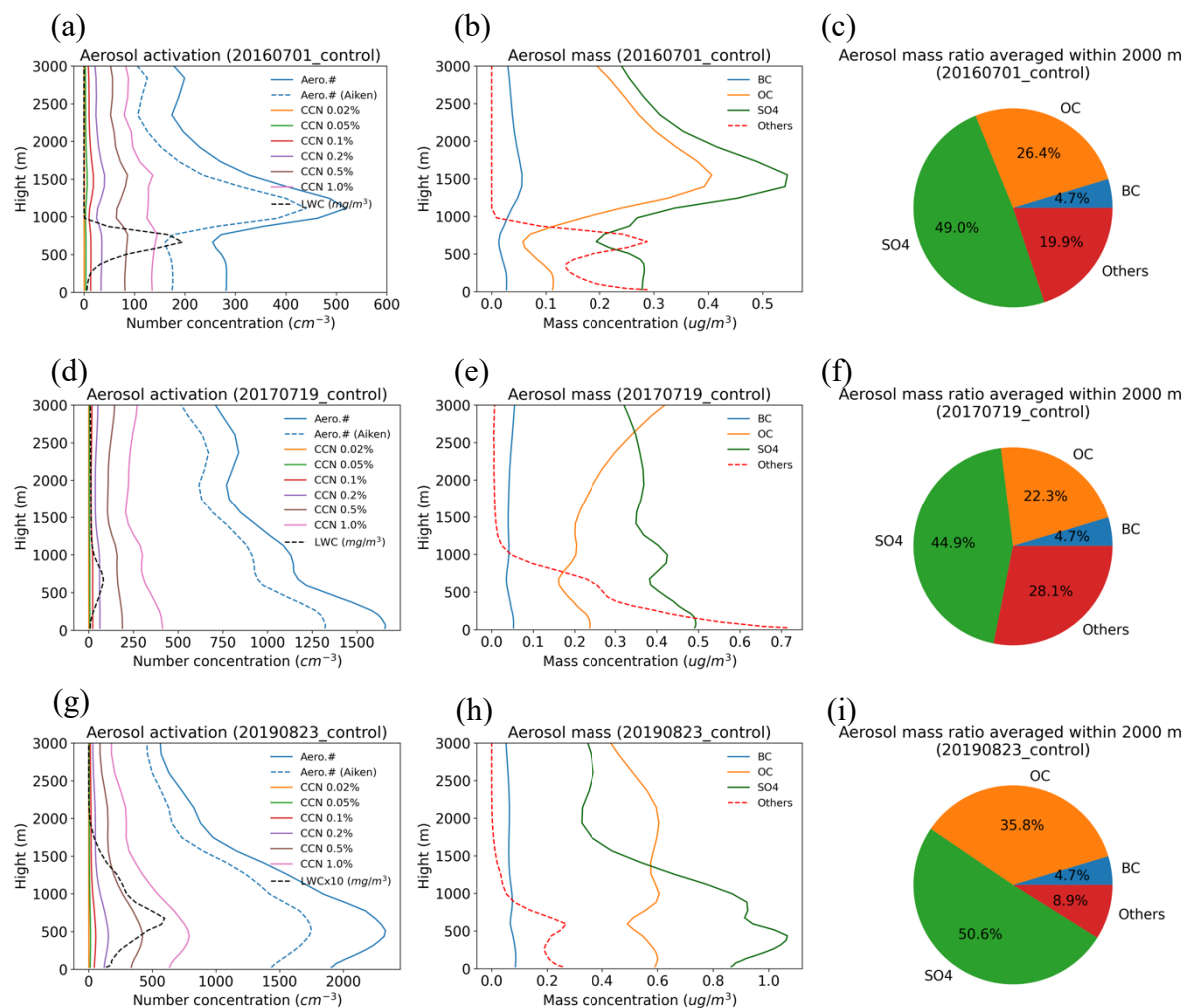
Figure 7. (a), (d), and (g) WRF-Chem vertical profiles of aerosol number concentration (Aiken mode and accumulation mode; units: cm^{-3}), aerosol number concentration (Aiken mode only; units: cm^{-3}), CCN number concentration below different supersaturations (units: cm^{-3}), and liquid water content (cloud and rain; units: mg m^{-3}) averaged over the domain 4 on 1 July 2016, 19 July 2017, and 23 August 2019, respectively, in the control runs. (b), (e), and (h) WRF-Chem vertical profiles of BC, OC, SO$_4$, and other species (like sea salt) (units: μg cm^{-3}) averaged over the domain 4 on 1 July 2016, 19 July 2017, and 23 August 2019, respectively, in the control runs. (c), (f), and (i) Pie chart of aerosol mass of different species averaged within 2000 m height on 1 July 2016, 19 July 2017, and 23 August 2019, respectively, in the control runs. Note that LWC is adjusted to fit the scale of x-axis for each case.
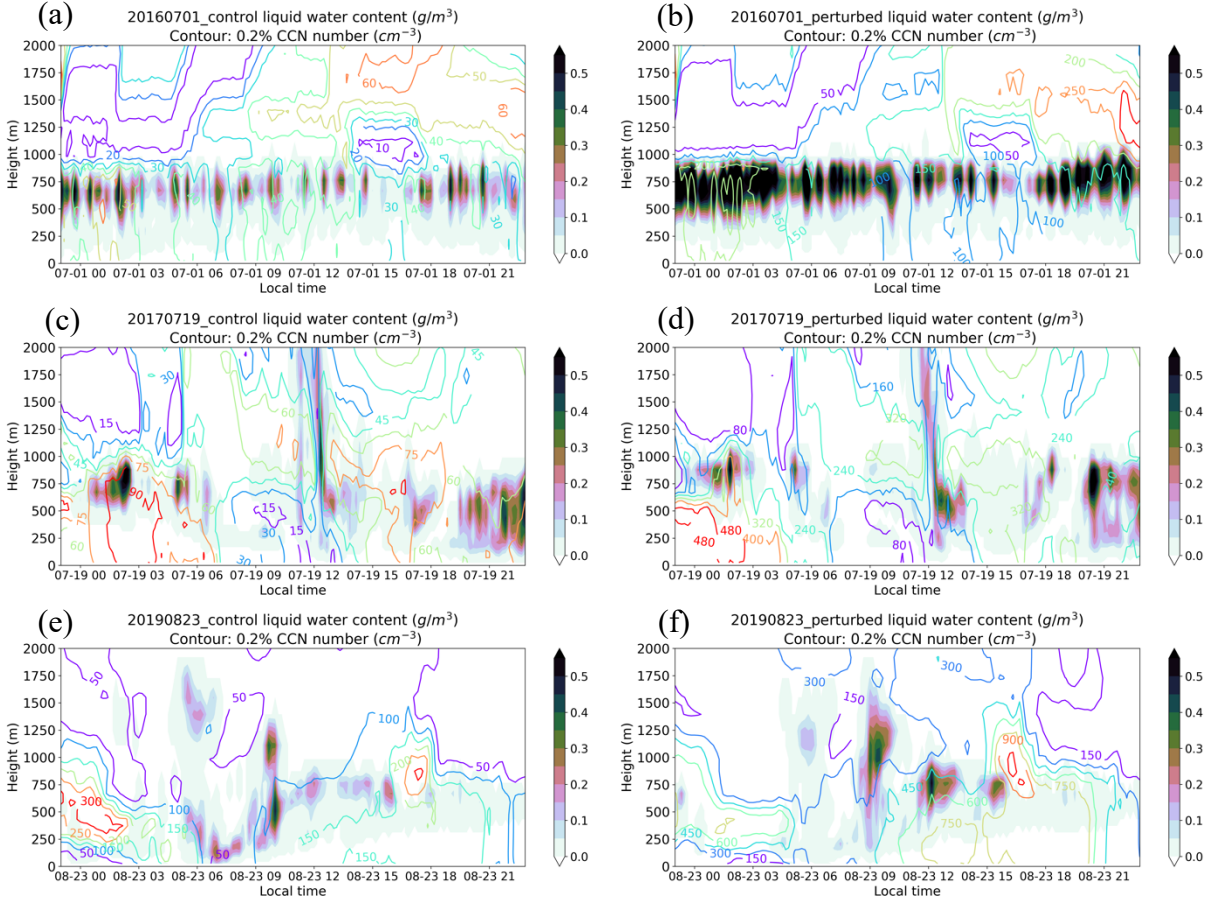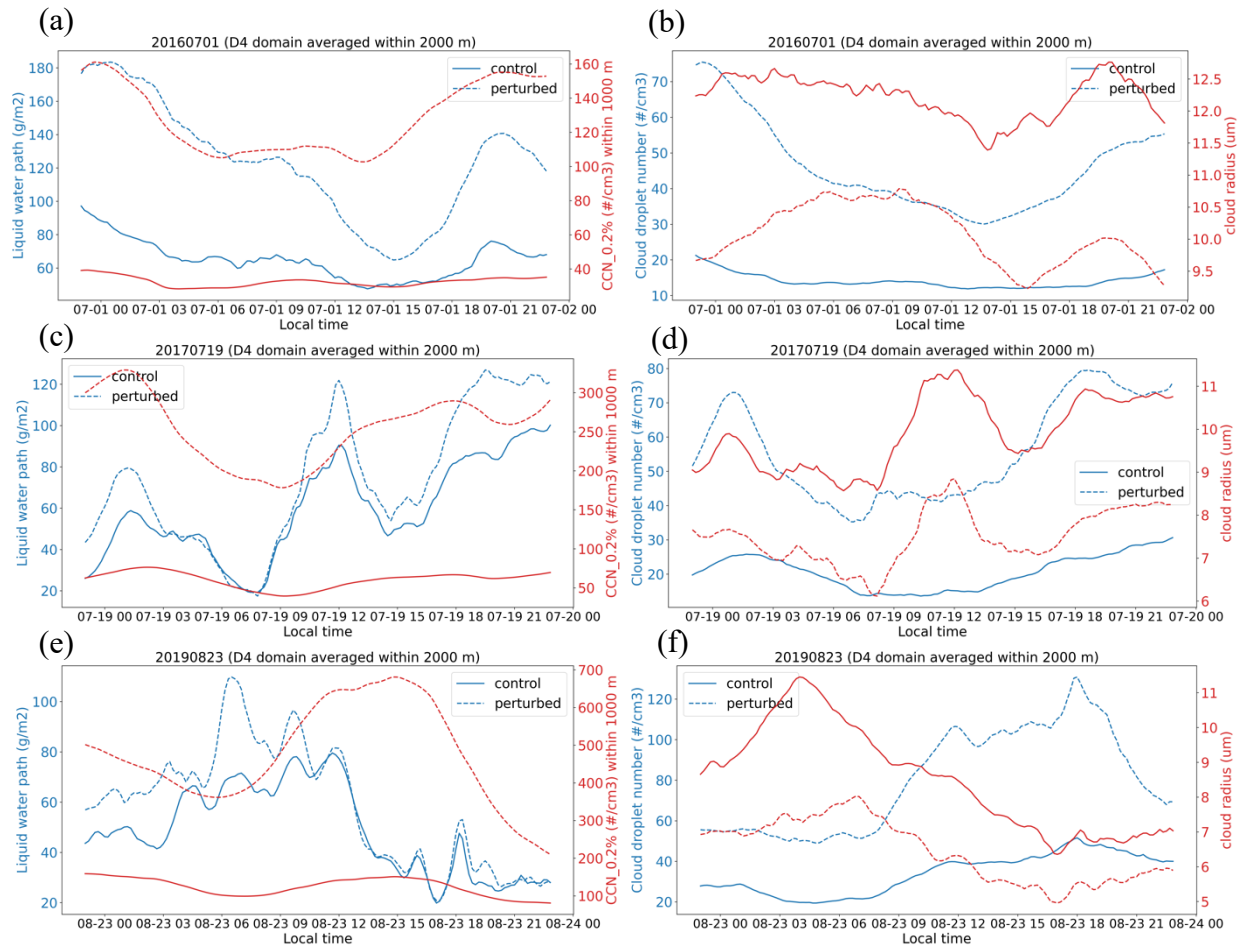
Figure 8. (a), (c), and (e) are the time series (local time; UTC – 1 hour) of 4 km-averaged cloud liquid water content profile (shade; units: g cm^{-3}) and CCN (0.2% supersaturation) number concentration profile (contour; units: # cm^{-3}) on 1 July 2016, 19 July 2017, and 23 August 2019, respectively, in the control runs. (b), (d), and (f) are the same as (a), (c), and (e), respectively, but in the perturbed runs. The data are averaged from the model simulated results over 20 × 20 grids centered on the Azores (approximately 4 km resolution).

Figure 9. (a), (c), and (e) are the time series of domain-averaged liquid water path (blue lines; units: g m^{-2}) and CCN number concentration below 0.2% supersaturation (red lines; units: # cm^{-2}) for the control case (soild lines) and the perturbed case (dashed lines) on 1 July 2016, 19 July 2017, and 23 August 2019, respectively. (b), (d), and (f) are the time series of domain-averaged cloud droplet number (blue lines; units: # cm^{-3}) and cloud radius (red lines; units: μm) for the control (soild lines) and perturbed (dashed lines) on 1 July 2016, 19 July 2017, and 23 August 2019, respectively. Only CCN data are averaged within 1000 m height over domain 4, other variables are averaged within 2000 m height.
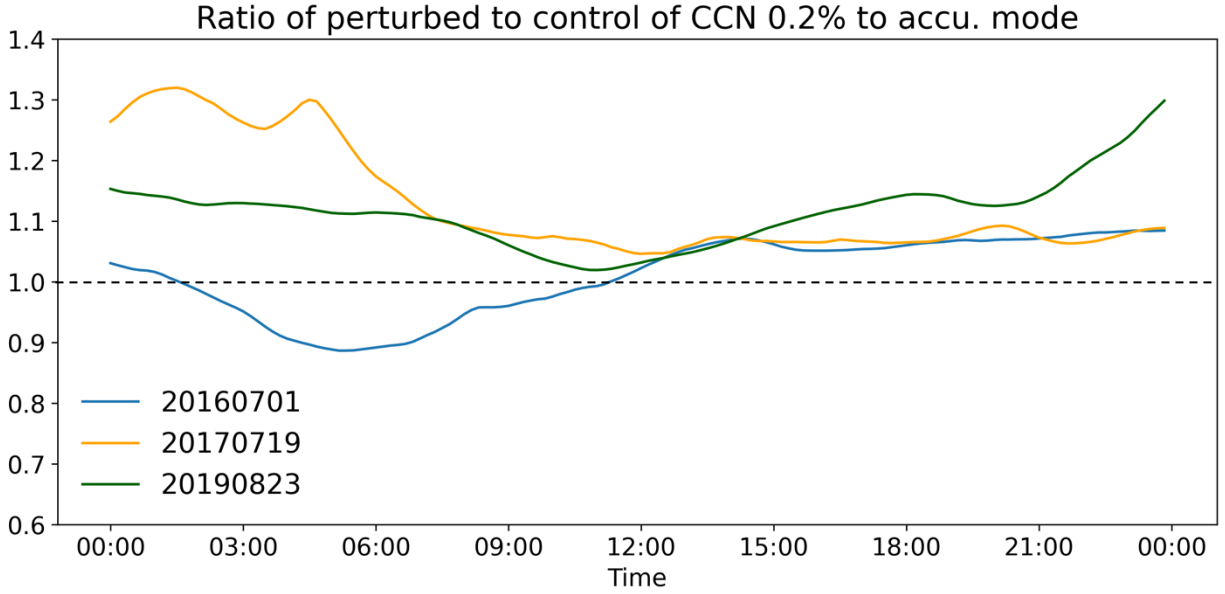
Ratio of perturbed to control of CCN 0.2% to accu. mode

1214
1215 Figure 10. The time series of the ratio of the number concentration of CCN at a supersaturation
1216 of 0.2% in the perturbed runs to that in the control runs, normalized by the corresponding
1217 accumulation mode aerosol concentration, defined
1218 as $\left.(CCN_{0.2\%}/Accu.\,aerosols)_{perturbed}\middle/(CCN_{0.2\%}/Accu.\,aerosols)_{control}\right.$. The black dashed
1219 line indicates the value of unity.
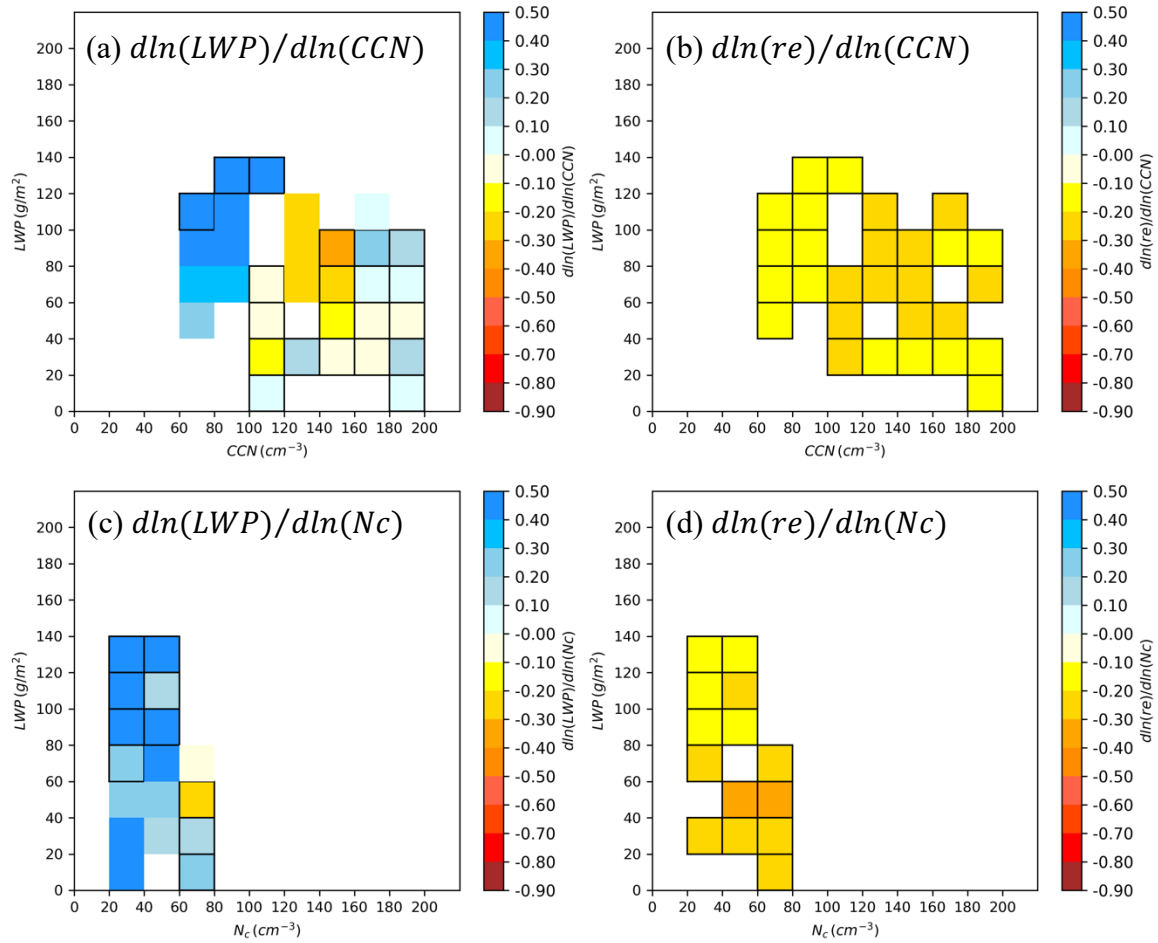1220

1221

1222

Figure 11. (a) and (b) are the mean liquid water path (LWP) and cloud radius (Re) susceptibilities for different cloud condensation nuclei (CCN) and LWP bins for three study cases, respectively. (c) and (d) are the same as (a) and (b), respectively, but for different cloud droplet number (Nc) and LWP bins. The logarithmic slope between LWP and CCN, denoted as $(dln(LWP)/dln(CCN))$, is calculated at each output time (every 10 minutes) using data from 16 aggregate grid points (~25 km for each grid point) from the control run and 16 aggregated grid points from the perturbed run. Black edges indicate statistically significant results with $p \leq 0.01$.
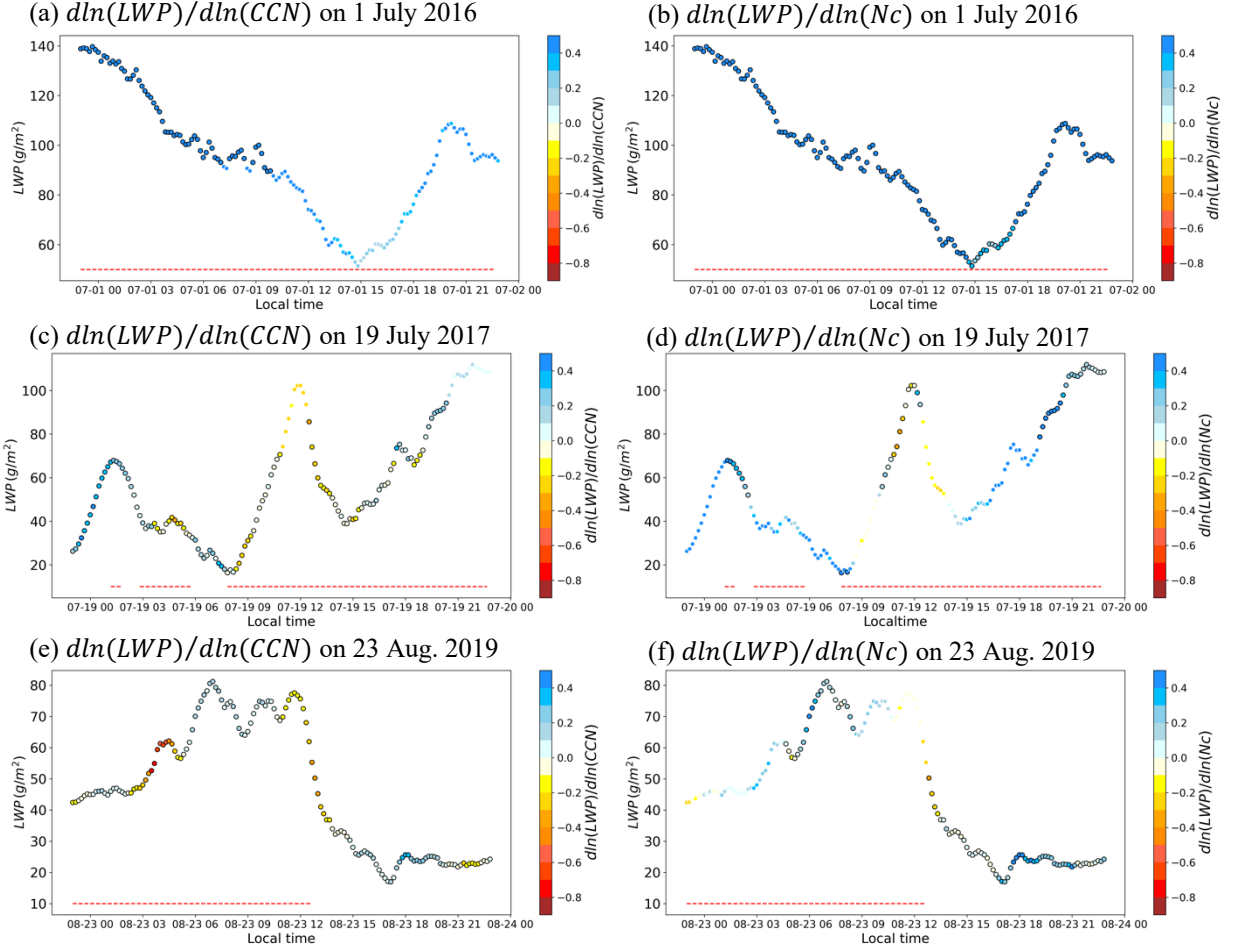
1232

1233

1234
1235 Figure 12. (a), (c) and (e) are the time variable of LWP susceptibility for different CCN
1236 concentration, denoted as ($dln(LWP)/dln(CCN)$), on 1 July 2016, 19 July 2017, and 23 August
1237 2019, respectively. (b), (d) and (f) are the time variable of LWP susceptibility for different Nc
1238 concentration, denoted as ($dln(LWP)/dln(Nc)$), on 1 July 2016, 19 July 2017, and 23 August
1239 2019, respectively. The logarithmic slope between LWP and CCN is calculated at each output
1240 time (every 10 minutes) using data from 16 aggregate grid points (~25 km for each grid point)
1241 from the control run and 16 aggregated grid points from the perturbed run. Black circles indicate
1242 statistically significant results with $p \leq 0.01$. The red dashed lines indicate when rainfall intensity
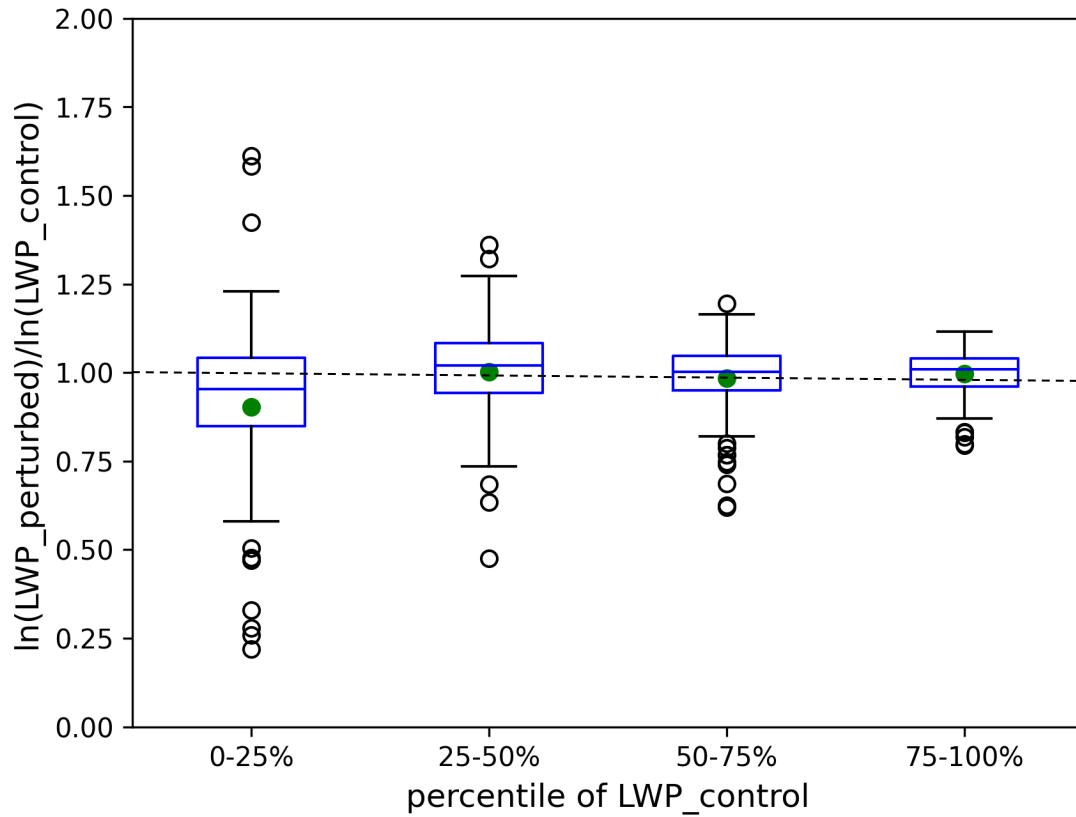1243 is higher than 0.001 mm 10-min^{-1} in domain 4.

1244

1245

1246

Figure 13. Boxplot of the relative change in $ln(LWP)$ between the perturbed and control cases across different LWP Percentile ranges in the control case during the negative susceptibility for LWP shown in Fig. 12. The box extends from the first quartile to the third quartile of the data, with a line at the median. The whiskers extend from the box to the farthest data point lying within 1.5x the inter-quartile range from the box. Outlier values are those past the end of the whiskers. Green dots are the mean value, and the back dashed line indicates the value of 1.0.

1247
1248
1249
1250
1251
1252

1253